Spring 2017

TiO2/PDMS Buoyant Photocatalyst for Water Remediation and Cu-RBS Organic/Inorganic Hybrid for Thermoelectric Applications

John R. Bertram
Western Kentucky University, john.bertram261@topper.wku.edu

TIO_2/PDMS BUOYANT PHOTOCATALYST FOR WATER REMEDIATION AND CU‑RBS ORGANIC/INORGANIC HYBRID FOR THERMOELECTRIC APPLICATIONS

A Thesis
Presented to
The Faculty of the Department of Chemistry
Western Kentucky University
Bowling Green, Kentucky

In Partial Fulfillment
Of the Requirements for the Degree
Master of Science

By
John Robert Bertram

May 2017

TIO$_2$/PDMS BUOYANT PHOTOCATALYST FOR WATER REMEDIATION AND CU-RBS ORGANIC/INORGANIC HYBRID FOR THERMOELECTRIC APPLICATIONS

Date Recommended 4/14/2017

Dr. Matthew J. Nee

Dr. Hemali Rathnayake

Dr. Jeremy Maddox

Dean, Graduate School 4/24/17 Date

To my wife, Beth. You have been nothing but encouraging towards my aspirations, and a solid foundation of support throughout this experience.

ACKNOWLEDGEMENTS

I would like to sincerely thank my research advisor, Dr. Matthew Nee, for his kindness and patience throughout my research experience. His understanding and enthusiasm for physical science has been an inspiration to me. I would also like to express my gratitude to my collaborator and committee member, Dr. Hemali Rathnayake, for introducing me to the exciting field of thermoelectrics and supporting me as a research assistant. I am also grateful to my additional committee member, Dr. Jeremy Maddox, for his insightful suggestions to improve my research.

Many thanks go to Dr. John Andersland for his instruction and training in scanning electron microscopy. I would like to thank Pauline Norris for her instruction using thermogravimetric analysis. I would also like to thank Mrs. Haley Smith for her help with administrative work within the chemistry department, and Mrs. Alicia Pesterfield for providing necessary reagents and equipment for my research. Special thanks to Aubrey Penn and Paige Huzyak for synthesizing the organic species used in my research. I am also very grateful to my friends at WKU and the chemistry department for their support and encouragement throughout this chapter of my academic career.

Last but not least, I would like to thank my parents who have always supported and believed in me. I also want to thank all my friends who encouraged me to work hard and achieve my goals.

TABLE OF CONTENTS

LIST OF TABLES

Table Page

LIST OF FIGURES

Figure Page

LIST OF SCHEMES

Scheme Page

LIST OF CHARTS

TIO_2/PDMS BUOYANT PHOTOCATALYST FOR WATER REMEDIATION AND CU-RBS ORGANIC/INORGANIC HYBRID FOR THERMOELECTRIC APPLICATIONS

John R. Bertram May 2017 97 Pages

Directed by: Dr. Matthew Nee, Dr. Hemali Rathnayake, and Dr. Jeremy Maddox

Department of Chemistry Western Kentucky University

Two novel materials have been developed: TiO_2/poly(dimethylsiloxane) (PDMS) beads as buoyant photocatalyst materials for water remediation, and copper rhodamine-B silane (Cu-RBS) as an *n*-type organic/inorganic hybrid for thermoelectric applications. The approach to incorporate TiO_2 into low-density PDMS beads addresses many of the challenges traditionally encountered when creating buoyant photocatalysts, an area which is crucial for wide-spread remediation of water resources, including natural bodies of water. The performance and reusability of the buoyant photocatalyst materials, demonstrated by using methylene blue as a model degradation target, is strong enough for environmental application. The use of a kinetic model and the introduction of a parameter to allow comparison of buoyant photocatalysts is also included as part of the analysis.

The performance of Cu-RBS was investigated as a low-temperature thermoelectric material. Clear improvements in the electrical conductivity and Seebeck coefficient are observed for RBS upon coordination to Cu^{2+}. Evidence explaining this improvement is provided by computational analysis and by concentration-dependent optical absorption and fluorescent emission measurements, all of which indicate that a metal-to-ligand charge transfer occurs from Cu^{2+} to RBS. Although the power factor of Cu-RBS is low compared to other materials reported in the literature, these results

provide a promising approach to increasing both the Seebeck coefficient and electrical conductivity of n^-type small molecule organic systems.

CHAPTER I

Introduction

1.1 Water Remediation and Photocatalysts

Water contamination comes in many forms and can have detrimental effects on animals, humans, aquatic life, and surrounding ecosystems. Among many concerns, the most pressing are human health, the unprecedented death of aquatic life, which disrupts food chains, and contraction of diseases caused from consuming contaminated water or aquatic life. From industrial runoff leaking carcinogenic dyes, to oil spills spewing toxic hydrocarbons, the range of harmful molecular species that enter the world's water supply is extensive.[1,2] There are many degradation processes that occur in nature such as biodegradation, decomposition, and photodegradation. However, many of the more harmful species are resistant to these removal pathways and experience long lifetimes in bodies of water.

Traditional wastewater treatment methods are lacking removal techniques that target these persistent organic pollutants. Most industrial and municipal water treatment plants carry out three successive processes, including phase separation, oxidation, and polishing. Phase separation consists of sedimentation of solids and dense, non‑polar liquids (which is the primary technique for sewage treatment) and/or filtration of fine solids through fine physical barriers. Oxidation is a secondary treatment method consisting of biochemical oxidation (digestion) or chemical oxidation, both of which only target bacteria and microbial pathogens. The final treatment process, polishing, is conducted in one of two ways: activated carbon is dumped into the treatment vat and removes pollutants by absorption, or sand filtration is used to remove remaining solids.

Unfortunately, none of these processes target water-soluble pollutants, such as methylene blue and rhodamine-B, which are known carcinogenic species often found in industrial waste streams.[3]

On the other hand, photocatalysts possess the capacity to absorb sunlight and ultimately mineralize the otherwise persistent pollutants into harmless small molecules, such as H_2O and CO_2. The photocatalytic degradation process is non-discriminatory towards pollutants and has been shown to rapidly remove trace amounts of organic compounds, both soluble[4] and insoluble.[5] However, their direct application into bodies of water results in a nano-fine suspension that is both costly and time-consuming to recover. This barrier can be overcome by implementing photocatalyst materials into buoyant substrates, allowing simple recovery and potential reuse of the photocatalyst material.

1.1.1 Overview of Photocatalytic Degradation Process

In 1985, Tanaka and co-workers[6] described a way to degrade persisting organic pollutants, in which TiO_2 was used as a photocatalyst to degrade aqueous phenols in the presence of UV light. Since its early description, photocatalytic degradation has been utilized to degrade a wide range of harmful species including aromatic hydrocarbons,[5] iodinated-contrast media,[7] microbial bacteria,[8] *etc.* The nondiscriminatory behavior of photocatalysts in elimination of pollutants makes them ideal candidates for treatment of contaminated water supplies and sources.[9] Their ability to harvest sunlight, a natural and renewable energy resource, as well as to resist consumption in the degradation reaction makes photocatalysts enticing candidates for water decontamination. TiO_2 is a particularly ubiquitous photocatalyst because of its low cost and environmental

inertness.[10-13] It is employed for various purposes; including self-cleaning surfaces,[14] and dye-sensitized solar cells,[15] both of which operate under the same general mechanism initiated by photo-activation of the semiconductor's charge carriers.

TiO_2 is classified as an *n*-type semiconductor, possessing an energy gap of ~3.2 eV (anatase)[16] between its valence band and conduction band, which comprise 2*p* O and 3*d* Ti orbitals, respectively.[9] The mechanism by which light activates TiO_2 in an aqueous environment is depicted in Figure 1.1. When a photon with a maximum wavelength of 387 nm strikes the surface of the photocatalyst, it is absorbed, transferring its energy to an electron in the 2*p* orbitals of O. This energetic electron is then excited into the 3*d* orbitals of Ti, leaving behind a positive entity, often referred to as a hole, or positron in the valence band. This electron-hole pair is commonly referred to as an exciton. The generation of an exciton within TiO_2 allows molecular species to react with the hole and electron through oxidative and reductive processes, respectively. For instance, the hole and OH^- react to form a hydroxy radical ($\cdot OH$) in solution by oxidation of OH^-, while the conduction band electron is attached to O_2 creating a superoxide anion radical (O_2^-). These short-lived, highly reactive radicals will attack proximal organic compounds, ultimately mineralizing them into biologically-inert molecular species such as H_2O and CO_2.

1.1.2 Current Methods of Application

Despite their impressive performance, the number of different methods in which photocatalysts have been used for water remediation is small. This is a direct result of the

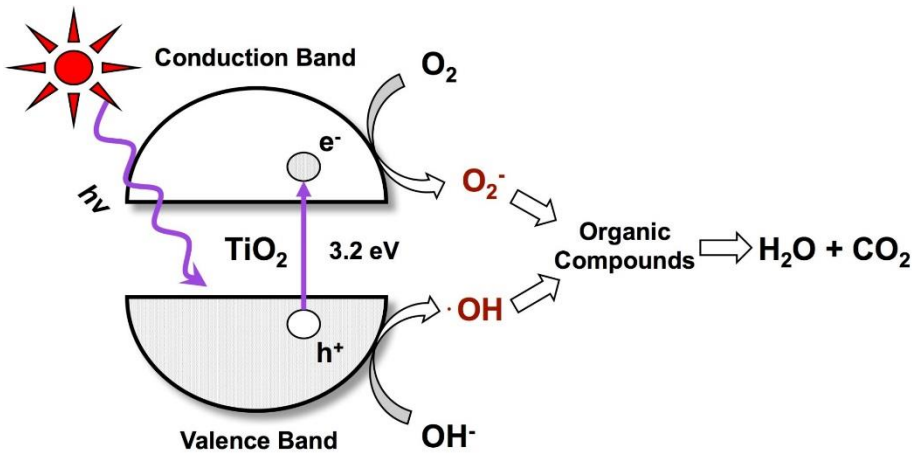

Figure 1.1: Light activation and photocatalytic degradation mechanism of titanium dioxide.

physical properties of most photocatalysts such as TiO_2, which forms a nano-fine suspension when introduced into water. Although their remediation performance in this heterogeneous form is exceptional compared to photolysis alone,[9] post-treatment recovery is time consuming and extremely difficult. To mitigate this, many previous works have focused on the deposition of a photocatalyst as a thin-film onto an inert substrate such as glass or quartz.[17] Often these films are placed into fluidic reactors for treatment of waste-water as part of municipal recovery plans.[18,19] Their potential in this method is noteworthy, but in terms of large-scale environmental cleaning, such as in recent disasters at the Deep-Horizon[20,21] and Elk River sites,[22] the use of dispersed or substrate-adhered photocatalysts is unfeasible. Instead, a buoyant substrate to anchor the photocatalyst would be advantageous and more practical for direct application to natural bodies of water.

1.2 Buoyant Photocatalyst Materials

Buoyant photocatalyst materials exhibit many desirable features compared to other application methods for various reasons: concentrating the photocatalyst at the liquid-air interface where most insoluble pollutants reside; providing direct exposure of the photocatalyst to sunlight, which experiences significant power loss deeper than 0.5 m in water,[23] maximizing photon-energy conversion efficiency; enabling simple post-treatment recovery using nets or skimmers to collect the photocatalyst material; minimizing loss of photocatalyst; and minimal exposure to aquatic life below the surface of the water.

Anchoring a photocatalyst to a buoyant support poses a single drawback. The generation of photooxidative species is dependent upon adsorption, as discussed in Section 1.1.2. Thus, attaching photocatalyst materials to a buoyant substrate will reduce the amount of surface exposed to the aqueous environment, and result in a diminishment of its performance. However, this can be balanced by the buoyant host material readily adsorbing the pollutants, which brings the contaminant molecules in proximity to the anchored photocatalysts.

1.2.1 Ideal Properties of a Buoyant Host-Material

In searching for materials to serve as buoyant host-matrices for a photocatalyst it is necessary to consider several features that are essential for the material to be a viable candidate. The material must be resistant to numerous degradation processes that could occur while employed, including photolysis by sunlight and oxidation or reduction reactions initiated by radical species generated from light activation of the photocatalyst.[24] A strong affinity between the photocatalyst and the host-material must

exist to ensure stable anchoring of the catalyst, preventing its release into natural environments. The host-material must also possess a strong affinity for the adsorption of pollutants, aiding in degradation by pre-concentrating the contaminants near the photocatalyst surface. A host-material that possesses a high surface area is ideal, maximizing direct exposure of the photocatalyst's surface to the aqueous environment. The buoyant photocatalyst material must also be stable for long periods of time, ensuring that the material can be reused for multiple degradation cycles.

1.2.2 Recent Progress in the Field

A variety of techniques have been demonstrated to achieve buoyancy without sacrificing high photocatalytic activity, as recently reviewed by Singh et al.[24] Polymer substrates remain strong candidates for adding buoyancy to conventional photocatalysts because of low cost and ease of morphological control. For example, photocatalytic sheets (where a thin layer of polymer is inoculated with a photocatalyst) have been shown to have reasonable success for degradation of model compounds like methylene blue (MB),[25] phenols,[26] and rhodamine-B (RB).[27] Many of the ideal properties of a host-material mentioned in Section 1.2.1 are exhibited by microporous PDMS beads. Sheets and other morphologies may not spread well over a large surface area of contaminated water. Beads are ideal in this situation because they spread without inhibiting oxygen uptake, they are easy to recollect after use, and they are easy to manufacture, ship, and store.

Polymeric materials with varying morphologies have been used as a buoyant host-material for photocatalysts in recent work. For instance, polyurethane foam was used by Zhang et al. as a TiO_2 substrate to reduce Cr^{4+} along with organic compounds

(RB, methyl orange, and MB).[27] Singh et al. chose polystyrene sheets as a TiO_2 substrate,[25] and in a former study modified TiO_2 by Ag^+-doping to delay electron-hole recombination within the photocatalyst.[28] Polystyrene was also used by Altın et al., embedded with ZnO in the form of beads, which was successful at removing both MB and the microorganisms *E. coli* and *A. niger* from an aqueous environment.[8] Polypropylene has been subjected to TiO_2 implantation in the form of fabric[29] and slab-like composite to serve as a buoyant support.[30]

Although polymers are frequently used as buoyant supports, photocatalytic aerogels have recently become an active area of research exhibiting high surface areas and low densities, properties which make aerogels well-suited for contaminant adsorption and subsequent degradation on aqueous bodies. Many have been fabricated for water decontamination including SiO_2/TiO_2 aerogel by Xu et al.,[31] and a novel C_3N_4/graphene aerogel capable of visible-light absorption reported by Wan et al.,[32] Brunnauer-Emmett-Teller (BET) analysis revealed these materials possess an average surface area of 533 $m^2 g^{-1}$ and 385 $m^2 g^{-1}$, respectively. Although their performances are formidable, aerogel fabrication techniques generally require extreme temperatures for calcination (>550 °C) and/or freeze-drying for stabilization (<–80 °C) which could hinder the commercial availability of such materials. The TiO_2/PDMS beads fabricated in this work possess the high surface area and low density advantages of aerogels but to a lesser extent: PDMS beads can reach surface areas up to 64.9 $m^2 g^{-1}$,[33] which is nearly the area of a typical two-bedroom apartment. However, unlike aerogels, the fabrication of

the polymeric beads requires temperatures of only 75 °C, eliminating concerns about unintended changes to the crystal structure of TiO_2.

1.2.3 Known Properties of Cross-linked Poly(dimethylsiloxane)

Our group[33,34] and others[35] have previously used microbubble fabrication techniques for PDMS to produce high surface-area-to-volume (SAV) ratio beads from a simple heat-bath curing method. Microbubble fabrication produces millimeter-scale beads (1–2 mm) with microstructures that can provide SAV ratios that exceed equivalent available areas for sheets. We have previously shown that the morphology can be further tuned by addition of an electrolyte,[33] although we do not adjust that in the results described here concerning the beads' use as a host-material. PDMS has several advantages as a polymer substrate: it is inexpensive, easy to produce, moldable, cures at low temperatures, and is both chemically and biologically inert enough for use in biomechanical devices. More notably, PDMS is frequently used in the concentration of organic traces from aqueous domains through sorption for use in solid-phase extraction applications,[36,37] and for separation and removal of crude oil from aqueous environments by adsorption.[38-40] This property is beneficial when serving as a buoyant substrate because it allows the preconcentration of insoluble pollutants near the surface of an anchored photocatalyst. PDMS has been previously used as a substrate for TiO_2 in microfluidic reactors,[10] but never as a substrate in a discrete buoyant photocatalyst. There have been successful studies in which TiO_2 has been coupled with PDMS for self-cleaning, super-hydrophobic surfaces and coatings which exhibit removal of organic dyes under UV radiation.[14,41,42] However, the range of application of these materials for removal of

harmful species in aqueous domains may be limited to environmentally-isolated reactors where buoyancy is not a necessity.

1.2.4 Cross-linking Mechanism of Poly(dimethylsiloxane)

The cross-linking mechanism of vinyl-terminated PDMS involves several sequential reactions, resulting in the eventual formation of a solid polymeric network. The cross-linking reactions, which have been identified and well-characterized,[43] are summarized in Scheme 1.1 for the specific reagents used in this study. As the cross-linking agent, triethoxysilane, is introduced into the emulsion, it immediately undergoes hydrolysis (Scheme 1.1(a)). An ethoxy group is cleaved and replaced with a hydroxide group attached to Si of triethoxysilane, leaving behind ethanol. The hydroxy-functionalized linker then initiates a hydrosilation reaction with a proximal PDMS chain (Scheme 1.1(b)), forming a new Si – C bond on either or both vinyl terminals. Once this occurs, two newly-functionalized neighboring PDMS chains can link via dehydration (Scheme 1.1(c)), resulting in an Si – O – Si linkage between them. These reactions propagate throughout the emulsion system, and a branched, cross-linked network of PDMS chains evolves. As the cross-linking density increases, the number of polymer chains that can slide past one another decreases. This causes the bulk PDMS material to gradually transition from a liquid to a solid material. This transition makes PDMS an ideal candidate for molding, and is why PDMS is often used for various lithographic applications.[43]

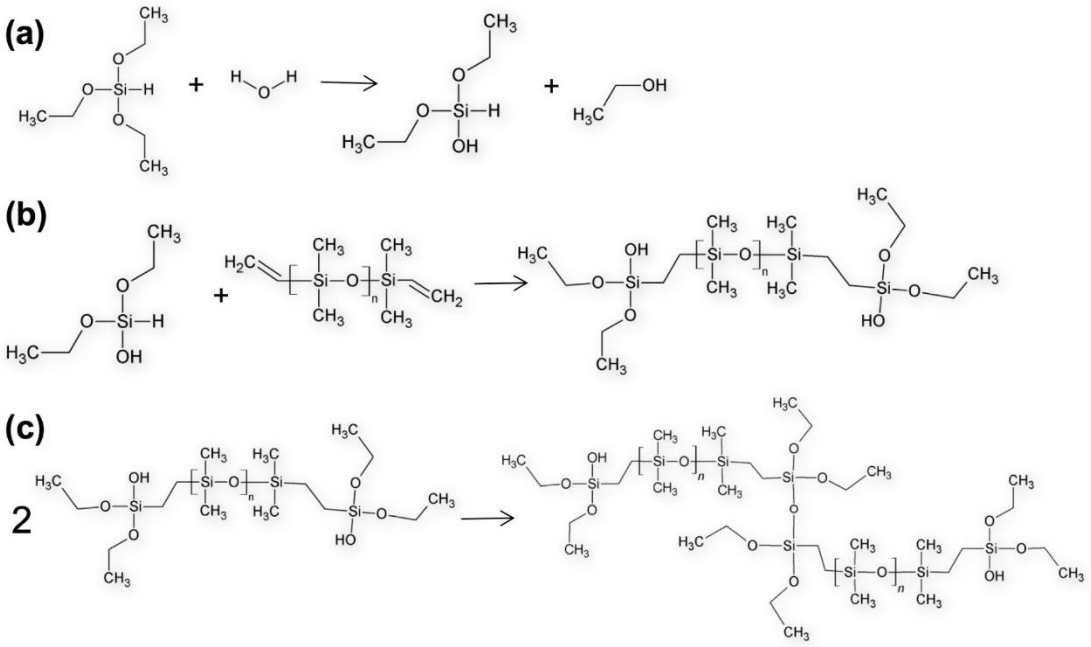

Scheme 1.1: Overall reaction mechanism for the cross-linking of PDMS chains in the presence of triethoxysilane. Triethoxysilane first undergoes (a) hydrolysis resulting in a hydroxy-functionalized siloxane species. This allows the siloxane monomer to undergo (b) hydrosilylation with a vinyl-terminated PDMS chain. Neighboring PDMS chains that have been functionalized can then cross-link to one another through (c) a dehydration reaction.

1.2.5 Overview

Our focus in the fabrication of TiO_2/PDMS beads is to (*i*) characterize this novel buoyant photocatalyst, and (*ii*) assess its performance in the removal of pollutants from water. Scanning electron microscopy is used to investigate the surface morphology of the inoculated beads, while energy dispersive spectroscopy (EDS) is used to provide the mass percent of TiO_2 anchored to the beads. Methylene blue (MB) is used as a model organic pollutant to test the removal performance of the buoyant photocatalyst. UV-visible absorption spectra are taken of MB in aqueous solution in various conditions: without any additives, with only TiO_2, with inert PDMS beads, and with TiO_2/PDMS beads (with and without UV exposure). The absorption intensity of MB is directly

proportional to its concentration; thus, we can measure the rate of reactions by recording the absorption peak area as a function of time. By implementing a kinetic model, this data is used to disentangle the various phenomena associated with MB removal in the presence of TiO_2/PDMS beads. This model is used to provide a rate constant associated only with MB removal by photooxidative species, which other work presenting novel buoyant photocatalysts found in the literature has not reported.

1.3 Thermoelectric Materials

Polymers are not only an attractive material for anchoring photocatalysts; they have been inoculated with a wide range of functional materials to improve certain properties depending on the specific application. For instance, light-emitting diodes (LEDs) were encased in the cross-linking polymer ethoxy bisphenol-A dimethacrylate for protection from oxidation in ambient air.[44] Polymers have also been used to provide flexibility and decrease the thermal conductivity of semiconductor materials for thermoelectric applications. For example, Te nanorods and Bi_2Se_3 nanoplates were embedded in a polyvinylidene fluoride matrix by Dun, et. al,[45,46] for wearable thermoelectric devices. In fact, thermoelectrics are a particularly attractive application for polymers because of their relatively low cost, mechanical flexibility, and large variety of demonstrated ways to tune electronic and thermal properties.[47] The remaining portion of this chapter is focused on a brief history of thermoelectricity, a discussion of key parameters in assessing a material's thermoelectric performance, and the benefits of harvesting thermal energy. Additionally, the desire for organic/inorganic hybrid systems as thermoelectric materials are discussed, along with recent progress in this field.

1.3.1 The Seebeck Effect

One of the electrical effects that heat energy can have on materials was first discovered by Thomas J. Seebeck in the early 19th century,[48] and is rightfully termed the Seebeck effect. Seebeck observed that materials can generate electricity through a temperature gradient; this effect has potential to serve as a means of generating electrical energy from waste heat, which is an otherwise untapped, renewable source of energy. This section entails a brief introduction to the Seebeck effect, a discussion of desirable materials properties for thermoelectrics, and a review of the advantages for harvesting waste heat.

Seebeck discovered in the early 1820's that by applying heat to a junction formed by two different metals, an electric potential was observed if the two metals were connected to a voltmeter. It was also observed that the amount of power produced by this thermoelement was directly proportional to the temperature gradient imposed on the two metals. Thus, the Seebeck coefficient of a single material at a given temperature is defined as

$$S = \frac{\Delta V}{\Delta T} \qquad (1.1),$$

Where S is the Seebeck coefficient, ΔV is the potential induced by the temperature gradient, ΔT, imposed on the material. Modern thermoelectric devices (representation shown in Figure 1.2) are usually composed of a series of unicouples containing a p-type material and a n-type material which are connected thermally in series, but electrically in parallel. When a temperature gradient (ΔT) is applied to a unicouple, an electro-motive force (or an open-circuit voltage) is observed that satisfies the relation

$$E_{np} = (S_p - S_n) \cdot \Delta T \quad (1.2),$$

Where E_{np}, S_p, and S_n are the open-circuit voltage and the Seebeck coefficients of the p- and n-type legs, respectively. The type of semiconductor (n-type, p-type, or intrinsic) is determined by its majority charge carriers, which can be determined by measuring the Seebeck coefficient. An n-type material, whose majority charge carriers are electrons in the conduction band, will induce a negative potential, and thus its Seebeck coefficient will be negative according to Eq. 1.1. The majority charge carrier of a p-type material is a positively charged hole, thus the potential induced under a temperature gradient will be positive, giving the Seebeck coefficient a positive value per Eq. 1.1. According to Eq. 1.2, a larger difference between the Seebeck coefficients of the n- and p-type material leads to a larger potential induced under a given ΔT. While a unicouple is not required to harvest thermal energy, having both n- and p-type semiconductors in a thermoelectric device drastically increases E_{np}.[49]

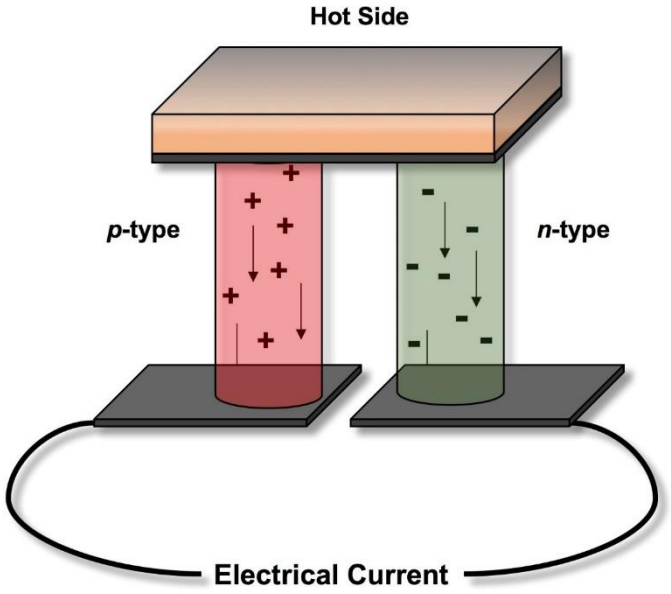

Figure 1.2: Schematic of a typical thermoelectric device demonstrating how a temperature gradient applied across a material facilitates charge-carrier flow.

1.3.2 The Thermoelectric Figure of Merit

The Seebeck coefficient is not the only variable necessary to evaluate a material's thermoelectric performance. In 1949 Abram Ioffe developed a comprehensive theory of thermoelectricity[49] and isolated an equation to define a material's thermoelectric performance using the 'figure of merit' (*ZT*),

$$ZT = \frac{\sigma \cdot S^2}{\kappa} \cdot T \qquad (1.3),$$

Where σ, *S*, κ, and *T* are the electrical conductivity, Seebeck coefficient, total thermal conductivity (a sum of the lattice and electronic contributions), and temperature of operation, respectively. $\sigma \cdot S^2$ of Eq. 1.3 is referred to as the power factor in the literature, and is usually provided in lieu of the *ZT* in cases where measurement of κ is unfeasible. Therefore, the primary goal of research in thermoelectric materials is to find or synthesize materials that possess a high electrical conductivity and Seebeck coefficient, while maintaining a low thermal conductivity. Unfortunately, all three parameters are temperature‐dependent and coupled together. A quantitative representation of the relationship of these three parameters with increasing carrier concentration by the Pisarenko relation[50] is depicted in Figure 1.3. Due to their wide band gaps, insulators have the largest Seebeck coefficients and the lowest thermal conductivity, but very poor electrical conductivity. The electrical conductivity increases with the carrier concentration, but a steady decline in the Seebeck coefficient is observed. The thermal conductivity and electrical conductivity are directly proportional, where an increase in carrier concentration results in an increased electronic contribution to the total thermal conductivity, which is governed by the Wiedemann‐Franz law.[51] The specific details of

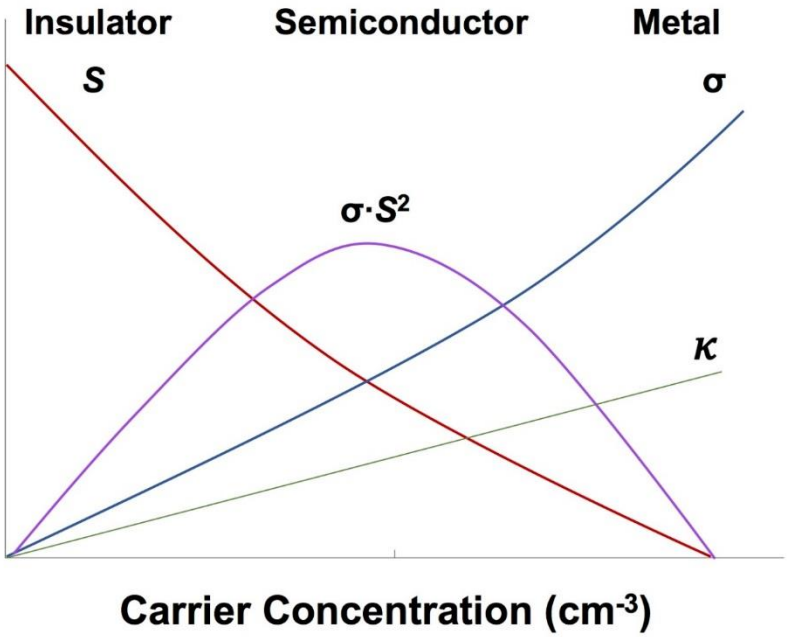

Figure 1.3: Depiction of the dependence of the electrical conductivity (σ), Seebeck coefficient (S), and thermal conductivity (κ) on the carrier concentration for solid state materials given by the Pisarenko relation.

phonon and charge-carrier transport theory goes beyond the scope of this work, however, it is clear that these three parameters must be balanced to achieve the highest possible *ZT* for a material.

1.3.3 Benefits of Harvesting Thermal Energy

A major application for thermoelectric materials is waste-heat recovery. It was pointed out by Vining[52] in his review that thermoelectric generators cannot compete with engine efficiency in the near future. In fact, many researchers acknowledge that thermoelectricity is not efficient enough to replace current power generation techniques.[50] Regardless, thermoelectric devices pose many advantages in terms of harvesting waste heat: no moving parts, quietness, compactness, and versatility. It is worth mentioning that 60% of energy in the U.S. is wasted in the form of heat.[50] While thermoelectric generators will not replace combustion engines, they can be coupled seamlessly with heat

generating sources to circumvent some of the otherwise wasted energy back into the system, ultimately reducing energy loss and improving efficiency of the overall system.

1.4 Organic/Inorganic Hybrids as Thermoelectric Materials

Apart from waste-heat recovery, many efforts have been focused on designing wearable devices powered by body heat for various applications; including sensing,[53] charging electronics,[54] and monitoring vital signs.[55] Organic semiconductors are promising materials for these applications, owing to their unique features in mechanical flexibility, ease of processing, low thermal conductivity, and easy tunability of optical and electronic properties through simple chemical modifications.[56-58] Solely inorganic devices reportedly possess higher *ZT* values than organic ones, but their implementation into wearable technologies is unfeasible due to their brittle, and usually toxic, nature.[59,60] Thus, the use of organic/inorganic hybrids as the active material in a thermoelectric device could overcome these limitations. An organic moiety introduced to an inorganic system provides mechanical flexibility with low thermal conductivity to an otherwise brittle material, while the inorganic counterpart provides additional charge carriers to the organic system.

1.4.1 Recent Progress in the Field

Of the organic thermoelectric systems presented in the literature, research investigating conducting polymers and their composites has emerged as alternatives to inorganic materials. Among them, *p*-type polymers and composites, especially derivatives of poly(3,4-ethylenedioxythiophene) (PEDOT), show a great promise for *p*-type thermoelectric properties with high power factors between 450-460 $\mu W \cdot m^{-1} \cdot K^{-2}$ at room temperature.[61] As mentioned in Section 1.3.1, both *n*- and *p*-type thermoelectric

materials are necessary to construct thermoelectric generators with high power output. However, reported power factors for flexible *n*-type organic thermoelectric materials are generally below 100 $\mu W \cdot m^{-1} \cdot K^{-2}$. An established approach to increase thermoelectric performance is by performing *n*-type doping which increases charge carrier concentration and therefore, charge transport properties of the material.[62] Despite this, many *n*-type semiconductors cannot be appreciably doped to achieve desired carrier concentrations due to their inherently low electron affinity.[63] Thus, efficient *n*-type organic thermoelectric materials are scarce in the literature. Among the few, metal-polymer coordination complexes are an example of flexible *n*-type materials undergoing investigation. Recently, the thermoelectric properties of three-dimensional copper 7,7,8,8-tetracyanoquinodimethane (Cu-TCNQ) coordinated polymer materials were investigated by Sun, et. al,[64] who reported a power factor of 2.5 $\mu W \cdot m^{-1} \cdot K^{-2}$. Additionally, an *n*-type coordination polymer containing nickel 1,1,2,2-ethenetetrathiolate (poly(K[Ni-ett])) fabricated by Sun, et. al,[65] exhibited a power factor of 26 $\mu W \cdot m^{-1} \cdot K^{-2}$. Hybrid super lattices composed of organic/inorganic moieties in the same unit cell have also been fabricated to exploit both desirable properties of organic and inorganic components. For example, the *n*-type TiS_2/[(hexylammonium)$_x$·(H_2O)$_y$·(DMSO)$_z$], fabricated by Tian et al.,[66] using an intercalation method, is a super lattice which exhibited a high power factor of 210 $\mu W \cdot m^{-1} \cdot K^{-2}$ at room temperature, showing promise for wearable thermoelectric devices.

Apart from metal/polymer complexes and hybrid super lattices, there are also ongoing searches for small molecule organic semiconductor systems that exhibit high

thermoelectric performance for use in flexible devices. Small molecule based systems possess several advantages when it comes to thermoelectric design: well-defined molecular structures, simple self-assembly into an ordered crystalline solid, and easy tunability of its electronic properties by chemical modifications. Additionally, it has been shown that long-range transport of charge carriers are possible in self-assembled layers of organic semiconductor systems.[67] Some of the most promising systems that have been investigated to date include phthalocyanines,[68] rubrene,[69] and pentacene.[70-72] Additionally, complexation of organic moieties with metal ions has proven to increase thermoelectric performance of molecular derivatives of porphyrines,[73] bis(terpyridine),[74] and bis(arylacetylide)[75] in which Zn, Fe, Co, and Ru ions were incorporated into their fused-arene systems.

1.4.2 Overview

Here, a novel organic/inorganic hybrid material has been designed for thermoelectric applications from a silanized rhodamine-B (RB) derivative and Cu^{2+} as a promising material for flexible heat-harvesting devices. To our knowledge, no former studies on the thermoelectric properties of the xanthene-based dye RB have been conducted to date. RB and its derivatives are appealing candidates for small molecule organic/inorganic hybrid systems due to RB's abundance, easy processing in the aqueous phase, simple approaches to molecular engineering of its side chains, and the reported ability of its derivatives to act as a Schiff-base ligand towards numerous transition metal ions.[76-78] We perform experimental studies of this novel complex as a thin film by investigating absorption and fluorescence properties in solution and in the solid-state,

and by measuring the electrical conductivity and Seebeck coefficient to calculate the power factor at room temperature. Theoretical simulations are also performed to yield key insight into this novel material by providing the most energetically favorable binding site of Cu^{2+} to rhodamine‑B silane (RBS), molecular orbital contours, electrostatic surface potentials, and molecular orbital energy levels. Derivatives of RB coordinated to transition metal ions, such as the one presented here, show promise as active materials in a flexible thermoelectric generator. The experimental methods and characterization techniques used are outlined in Chapter 2, with results presented in Chapter 4.

CHAPTER II

Materials and Methods

This chapter outlines the materials and techniques used to fabricate and characterize novel materials for applications in waste heat generation as well as water remediation. The fabrication and subsequent characterization processes remained the same for all PDMS bead samples and thin film devices unless otherwise specified in the respective results sections.

2.1 Materials and Reagents

For fabrication of PDMS beads with and without varying morphologies, vinyl-terminated poly(dimethylsiloxane) (Mw ~25,000), triethoxysilane, sorbitan monooleate, *n*-heptane, platinum (IV) chloride, zinc (II) chloride, and sodium chloride were purchased from Sigma-Aldrich, St. Louis, MO and were used without further processing. All aqueous solutions were prepared using deionized water (~18 MΩ). Sonication was performed in a 2.8-L VWR water-bath sonicator. Titanium (IV) oxide (nanopowder, < 21 nm) in its anatase form was also purchased from Sigma-Aldrich and used to create the buoyant photocatalyst materials. Methylene blue, used as the model degradation pollutant, was purchased in powder form from Sigma-Aldrich. A 300-W Xe-arc lamp (Newport, 66902) was used to irradiate a 50-mL quartz round-bottom flask containing the contaminant solution and buoyant photocatalysts. The solution was pumped through Tygon E-lab tubing using a peristaltic pump, both purchased from Cole-Parmer, into a quartz flow cuvette. A white-light LED and USB 2000 visible

spectrometer equipped with fiber optic cables from, all from Ocean Optics, were used to collect absorption spectra of MB.

Rhodamine-B silane (RBS) was synthesized by Aubrey Penn, the procedure for which can found in work recently published.[79] Polyhedral oligomeric silsesquioxane-anthracene (POSS-ANT) was synthesized by Huzyak, et. al,[80] the procedure for which can be found in their paper. Rhodamine-B, copper (II) nitrate, calcium nitrate, and 2-propanol used in thermoelectric device fabrication were purchased from Sigma-Aldrich. The indium-tin-oxide-coated square glass slides (25 × 25 × 1.5 mm) used as a thin film substrate for thermoelectric devices were also purchased from Sigma-Aldrich.

2.2 Materials Fabrication

2.2.1 PDMS Beads

1.04 g of PDMS and 1.02 mL of *n*-heptane were added to a 20-mL glass vial and subjected to 1 min of sonication to ensure solvation of the PDMS chains. 2 drops of sorbitan monooleate was then added to the vial along with 750 mL of DI water. The glass vial was sealed and shaken vigorously to initiate emulsion formation. The vial was submerged in an 800-mL beaker located in the water-bath sonicator containing an ice bath. A total of eight sonication periods were completed, lasting for 7 min each. The ice bath is maintained at or below 3° C throughout sonication to ensure stability of the emulsion.

To initiate cross-linking of PDMS in the emulsion, 5.4 mL triethoxysilane was slowly poured into the emulsion vial from a test tube. A glass stir rod was used to slowly

stir the mixture immediately after addition of cross-linker. After 2 min, the cross-linking emulsion was added drop-wise to an aqueous solution of sodium dodecyl sulfate heated to 75° C, resulting in bead formation by heat curing. For those emulsions using various chloride salts, 0.03-M solutions of $PtCl_4$, $ZnCl_2$, and NaCl were substituted for a portion of DI water in emulsion contents, the amount of which was varied depending on the amount of salt content desired.[33] To incorporate TiO_2 photocatalyst into the PDMS beads, 0.05, 0.1, and 0.2 g of TiO_2 was added to the emulsion, corresponding to 5, 10, and 20% photocatalyst load with respect to the initial weight of PDMS. TiO_2 was added to approximately 3 mL of the emulsion mixture prior to sonication. After curing, beads were dried and rinsed with hexanes, then with water, prior to analysis or photocatalytic testing.

2.2.2 Preparation of Thin Film Devices

Glass substrates coated with ITO were thoroughly cleaned prior to thin film deposition. First, substrates were washed by sonication in dichloromethane for 10 min in a water-bath sonicator, followed by rinsing with deionized (DI) water, after which, the ITO substrates were immersed in ammonium hydroxide and hydrogen peroxide for 15 min at 50-70°C. The plates were then sonicated in DI water for 15 min and blown dry with argon gas, then subjected to UV radiation from a 300-W Xe-arc lamp for 35 min to remove any traces of organic compounds. RBS (15 µmol) and $Cu(NO_3)_2 \cdot 3H_2O$ (15 µmol) were added to 2 mL of 2-propanol in a glass vial and magnetically stirred for 1 hr at 70 °C.

For the glass substrates, tape was used to mask approximately half of the coated ITO, creating a cell area of 1.4 cm^2 for deposition of the active layer. Layers of the

sample solution were deposited on the masked ITO substrate by spray-coating the solution (2 mL) using an airbrush (Paasche, H0513). To maintain a consistent thickness between samples, twenty swift passes were carried out at 20 cm while keeping the pressure of the carrier gas, Argon, at 270 kPa. For the cathode, substrates with their active layers were subjected to thermal metal vapor deposition (TORR, FTM-2000) of Cu under a vacuum of 7 μTorr at a thickness of ~100 nm. Control devices of RBS only, RB only, and RB with Cu^{2+} (Cu-RB) were made in the same manner for comparing the performance of test devices made with RBS and Cu^{2+} (Cu-RBS). Ca^{2+} was also used in place of Cu^{2+} as a control to assess the ionic strength effect on electrical conductivity. Multiple devices composed of Cu-RBS, Cu-RB, RBS, and RB were fabricated to get statistical averages and standard deviations, ensuring reproducibility of data.

2.3 Materials Characterization

2.3.1 Microscopy

Surface morphologies of all PDMS beads were imaged using a scanning electron microscope (SEM, JSM-6510LV). The beads produced with $PtCl_4$, $ZnCl_2$, and NaCl were observed in the SEM in low vacuum mode with an accelerating voltage of 15 kV. Beads with TiO_2 anchored onto their surface were Au sputter-coated (EMSCOPE, SC500) prior to SEM analysis at an accelerating voltage of 20 kV. Energy dispersive spectroscopy (EDS, iXRF 550i) was used to perform elemental analysis to detect TiO_2 or salt content depending on the types of PDMS beads under investigation.

A light microscope was used to image PDMS beads containing RBS and POSS-ANT. A He-Xe UV lead light was fashioned with a 340 nm band pass filter to

induce fluorescent emission of the chromophores and provide their location within the PDMS beads.

2.3.2 Spectroscopy – UV/Vis, Fluorescence Emission, and Raman

The photophysical properties of RB, RBS, Cu^{2+} and RB (Cu-RB), and Cu^{2+} and RBS (Cu-RBS) in 2-propanol were studied using a fluorescence spectrometer (Perkin Elmer, LS 55) and UV-visible spectrometer (Shimadzu, UV-2600 Spectrophotometer). A concentration of 1.68×10^{-14} M mol/L was used for fluorescence measurements of RB, RBS, Cu-RB and Cu-RBS at a 1:1 chromophore to Cu^{2+} mol ratio. Absorption measurements were conducted at a concentration of 9 μM for RB, RBS, Cu-RB, and Cu-RBS at a 1:1 chromophore to Cu^{2+} mol ratio using pure 2-propanol as a blank. Cu^{2+} concentration was incrementally increased by 25 mol% from 0 to 100 mol% to investigate the fluorescence and absorption dependence (in separate solutions) of RBS in the presence of varying amounts of copper ions. Thin film UV-visible absorption measurements (Shimadzu UV-2600 Spectrophotometer) were carried out by spray coating solutions of RB, RBS, Cu-RB, and Cu-RBS onto transparent, square glass slides (25 × 25 mm) using the same procedure detailed in Section 2.2.4. A coated glass slide was then taped flush to the sample cuvette holder within the UV-vis spectrometer, while a plain glass slide was used as the blank.

A back-scatter Raman spectrometer (Agiltron, Desktop L-Peakseeker) with a spectral range of 200-3000 cm^{-1} was used as a fast, non-invasive technique to detect the presence of TiO_2 and to ensure its anatase crystal structure within PDMS beads before and after degradation experiments remained intact. Solid samples of TiO_2, PDMS,

TiO_2/PDMS, and TiO_2/PDMS after one degradation trial were packed into the corner of clean, unused plastic bags. The spectrometer tip was then placed inside a small black-out apparatus to avoid interferences with overhead lighting. The tip was held against the bag by using a small clamp while measurements performed in the dark.

2.3.3 Electrical Conductivity Measurements

The ITO coated surface was used as the anode and the Cu layer deposited onto the active layer was used as the cathode. The channel length between the two source meter (Keithley, 2400) probes was kept constant at 1.25 cm while the active cell area was maintained at 1.4 cm^2. Conductance of samples was calculated from the slope of the I-V curves and conductivities were obtained from

$$\sigma = \frac{\rho \cdot l}{a} \tag{2.1}$$

Where σ is electrical conductivity, ρ is conductance, and l and a are channel length and area, respectively. Each sample was tested five times to ensure reproducibility of the results.

2.3.4 Seebeck Coefficient Measurements

Measurements to calculate the Seebeck coefficient were conducted in a custom-built apparatus using a ceramic block heated in a vacuum oven to the desired hot-side temperature. After 15 min at this temperature, the block was placed on the underside of a device's active layer directly over one of the probes leaving the other end exposed to room temperature (~25 °C). The voltage induced by the temperature gradient (ΔT) at zero current density was measured directly from the device while maintaining the temperature of the cool side of the device at ~25 °C. The Seebeck coefficient (S) is the

slope of the thermovoltage (V) vs. the temperature gradient (ΔT, in K) plot, at current density $J = 0$.

2.4 Degradation Performance Experiments

2.4.1 Experimental Setup and Conditions

To assess the removal performance of the TiO_2/PDMS beads a flow system was implemented to avoid complications taking UV-Visible absorption measurements in the presence of the opaque beads and to isolate the UV-visible spectrometer in the dark to hinder interference from the high-power light source used to simulate sunlight. This setup is depicted in Figure 2.1. The 30-μM MB solution containing 0.3 g of buoyant photocatalyst was slowly stirred in a 50-mL quartz round-bottom flask with a magnetic stir bar under UV-Visible light irradiation from the 300-W Xe-arc lamp. A peristaltic pump with Tygon tubing was used to flow the MB solution (~50 mL min^{-1}) through a quartz cuvette. The quartz cuvette was isolated in the dark and placed between a white light LED source and UV-visible detector which records the absorption spectrum of MB *in situ*. Absorbance measurements were recorded at 5-min intervals over the course of 3 h. Control experiments using an MB solution without any additives were performed to assess the photolysis rate of MB. Also as a control experiment, inert PDMS beads (without any photocatalyst) were added to MB solutions to assess the extent of the effect that the opacity of the PDMS beads has on the direct photolysis of MB. To disentangle the various phenomena responsible for MB removal, further control experiments were performed in the dark to assess the extent of MB adsorption onto the PDMS beads (with and without TiO_2) without UV-light exposure. Suspensions of TiO_2 in MB solution of

the same concentration were exposed to UV light to compare the beads' performance to a dispersed photocatalyst. Under the same conditions, wavelength-dependent reflectance measurements of the solution were recorded to assess the photocatalytic degradation of MB. To confirm the validity of the reflectance measurements, similar trials were performed using inert PDMS beads instead of TiO_2. The resulting rate constants of MB degradation were within uncertainties of the values reported for absorbance measurements, confirming wavelength-dependent reflectance measurements are a sound method of comparison when absorbance is not feasible. Reflectance is not used throughout trials due to the larger signal to noise ratio compared to absorption measurements, which could result in further uncertainties associated with these measurements.

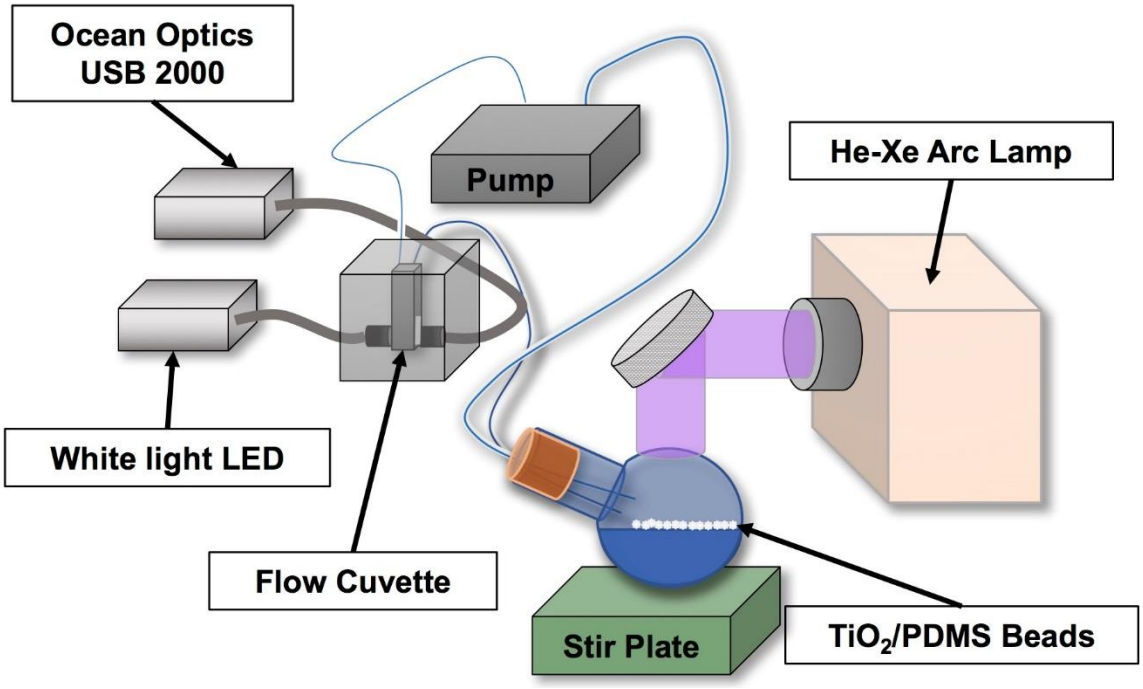

Figure 2.1: Experimental setup that allows monitoring of degradation of MB in real-time.

2.5 Computational Analysis

2.5.1 Cu^{2+} and Rhodamine-B Silane

All computational chemistry calculations were performed using the Gaussian 09 package[81] and their output files analyzed and visualized using GaussView 05 software.[82] First, the molecular structure of RB was optimized using the Becke three-parameter Lee-Yang-Parr (B3LYP) functional[83] and the split-valence 6-31G basis set.[84] An electrostatic potential (ESP) surface was generated in GaussView to identify potential Cu^{2+} binding sites and is depicted in Figure 2.2(a). RB geometry was re-optimized using the same approach, but with a Cu^{2+} ion placed in ten different locations around the molecule indicated in Figure 2.2(b). For these calculations, a split-basis set was applied to use the Los Alamos National Laboratory 2 Double-Zeta (LANL2DZ) pseudo-potential[85] for Cu^{2+} (because of its ubiquity in modeling heavy atoms) and 6-31G for all other atoms. Additional calculations were used to inspect the effect of Cu^{2+} positions including the use of 2-propanol as an implicit solvent, and using a more diffuse

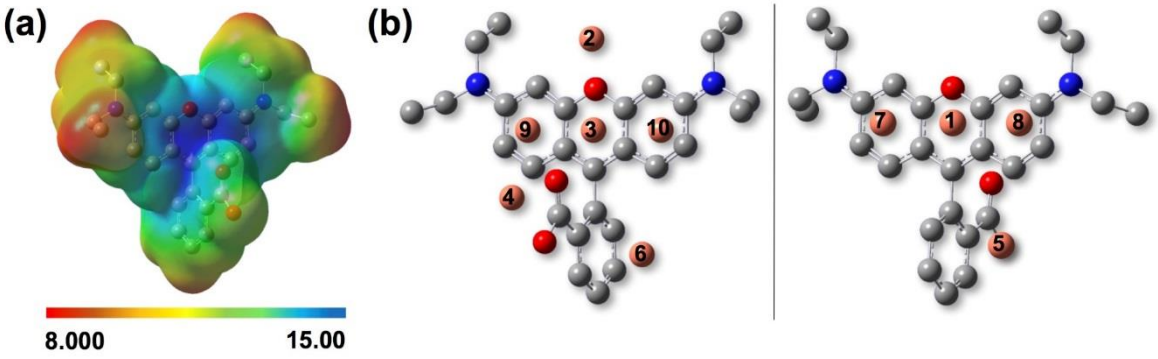

Figure 2.2: (a) ESP of RB and (b) various Cu^{2+} ion positions prior to geometry optimization using the B3LYP method and LANL2DZ basis set for Cu^{2+} and 6-31G for all other atoms.

basis set (6-31+G) to consider the outer reaches of the atomic radii. Despite these alterations, there was no change in the ordering or relative energy differences between positions nor the optimized positions of Cu^{2+} ions around RB and RBS, thus neither alteration was included in further calculations in the interest of efficiency.

The structure of RBS was constructed from the optimized structure of RB, then its geometry was optimized using B3LYP/6-31G. Based on the electron distribution of RBS (Figure 2.3(a)), Cu^{2+} ions were then placed in eight varying locations as depicted in Figure 2.3(b). This was followed by geometry optimization using the same method and mixed basis set (applying LANL2DZ to Cu^{2+} ion and 6-31G for all others) to assess the relative energies of their final positions.

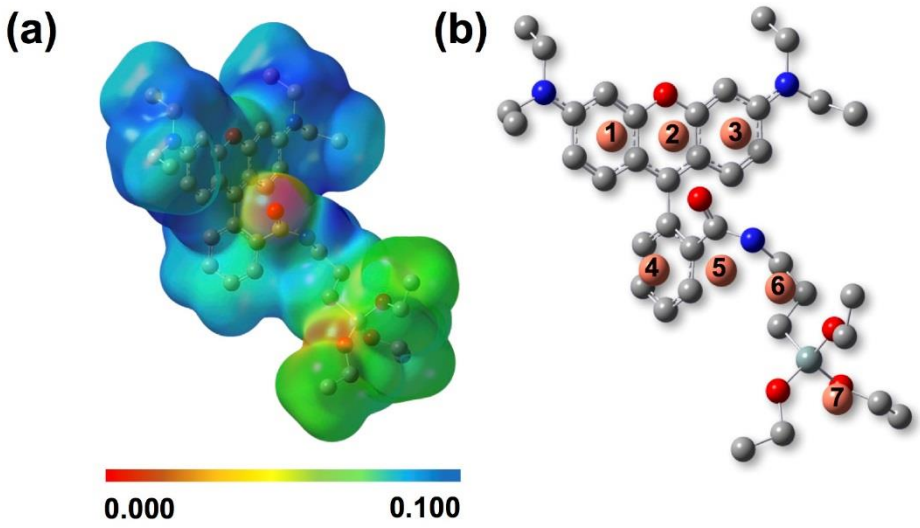

Figure 2.3: (a) ESP of RBS and (b) Cu^{2+} starting positions chosen prior to geometry optimization to find the most likely binding site of the metal on. The B3LYP method was used while LANL2DZ basis set was used for Cu^{2+} and 6-31G for all other atoms.

CHAPTER III

TiO_2/PDMS Buoyant Photocatalyst Results and Discussion

3.1 Physical Characteristics of Poly(dimethylsiloxane)

Poly(dimethylsiloxane) (PDMS) is a ubiquitous polymer due to its low-cost, biocompatibility, non-toxicity, and molding properties. The further expansion of PDMS's various uses is explored and analyzed in the following sections of this chapter. Potential applications studied revolve around the formation of PDMS by heat curing into a specific type of solid morphology, which possesses a high surface-area-to-volume ratio (SAV). The applications explored include an adsorptive substrate for analytical techniques such as solid-phase micro-extraction (SPME) a buoyant host material for photocatalysts in water remediation, and hosting conductive species to generate electricity from waste-heat energy.

3.1.1 Bead Morphology

PDMS is commonly used as an adsorptive substrate for extraction of nonpolar analytes in several analytical techniques, including solid-phase microextraction (SPME).[36,37] In these techniques, the performance of the fibrous substrate is directly proportional to its surface-area-to-volume (SAV) ratio. The more adsorptive capacity the material has per unit volume, the more analytes can occupy the surface of the SPME fiber. A technique to produce a high SAV morphology of PDMS was adopted by DuFaud et al.,[35] in which PDMS was dispersed in water as an emulsion via high-power sonication. The emulsion is rendered stable by a lipophilic surfactant and *n*-heptane mixed in with PDMS to tune the viscosity to near that of water. Once stability of the

emulsion is achieved, cross-linking of the polymer is initiated *in situ*. This is almost immediately followed by a drop-wise addition into a heat-tempered bath containing a hydrophilic surfactant, which serves to reduce the surface tension of the water. As the emulsion droplets enter the bath, they heat cure into a solid structure. These polymeric materials form by agglomeration of the microbubbles into clusters of tiny spheres of cross-linked PDMS, referred to as beads. Figure 3.1(a) contains a scanning electron microscope (SEM) image of a typical PDMS bead that was fabricated in our work where tiny spheres of PDMS are observed to contribute to the overall morphology. The beads possess a high SAV owing to their convex surface structure and porous matrix.

In their report, DuFaud et al., concluded that this high-SAV morphology was a direct result of emulsion formation prior to cross-linking initiation.[35] PDMS chains within individual droplets first begin cross-linking with themselves. Because the liquid polymer is dispersed in a small volume of water, neighboring polymer microbubbles will easily become agglomerated and linked by PDMS chains near their outer edges. Then, when introduced to the heated water bath in the form of a droplet, the cross-linking PDMS network fuses into a solid material, retaining the morphology of the emulsion and producing beads with a convex, bulbous surface morphology.

3.1.2 Morphology Manipulation Using $PtCl_4$

Previous work in our group had shown that dissolving platinum (IV) chloride ($PtCl_4$) into the emulsion prior to cross-linking drastically alters the morphology of the PDMS beads.[34] In that report, rather than a convex, bulbous surface, concave sites are observed with porosity throughout the solid matrix. An example of this alteration can be

seen in Figure 3.1(b), which depicts a PDMS bead fabricated in this work with aqueous $PtCl_4$. In that work, elemental analysis of domains within the SEM images indicated that platinum was found almost exclusively within the concave sites before washing the PDMS beads. Because Pt was found at centers of concave sites in the cured PDMS beads, this implied a catalytic role for the transition metal ion in the curing process rather than an incorporation. In fact, $PtCl_4$ is frequently used to catalyze hydrosilylation reactions which is used in a commercial PDMS curing kit manufactured by Dow Corning to decrease curing time.[86] The introduction of a salt must alter the surface tension of the emulsion bubbles formed in some regions, causing the continuous phase to cavitate within the discrete phase, which leaves behind concave sites once cured in the heated bath. However, because the addition of an electrolyte will increase the ionic strength, which may not be ruled out that the addition of a salt may alter the aqueous/aliphatic interface as well. The overall size of the microbubbles that form the emulsion seem to be reduced in the presence of the electrolyte. Based on the size of the spherical substructures in the SEM images, the microbubbles appear to be between 1-10 μm for beads without the addition of an electrolyte, where those fabricated with $PtCl_4$ are on the order of 0.2-2 μm.

3.1.3 Effects of $ZnCl_2$ and Brunaur-Emmett-Teller Analysis

The focus of this study was to determine if cheaper, more earth-abundant metal-salts could be used to induce a similar morphology and to further explore whether ionic strength of the emulsion or catalytic activity of the metal-ion were the determining factors. Zinc (II) chloride ($ZnCl_2$) was used as a replacement for $PtCl_4$, and proved to

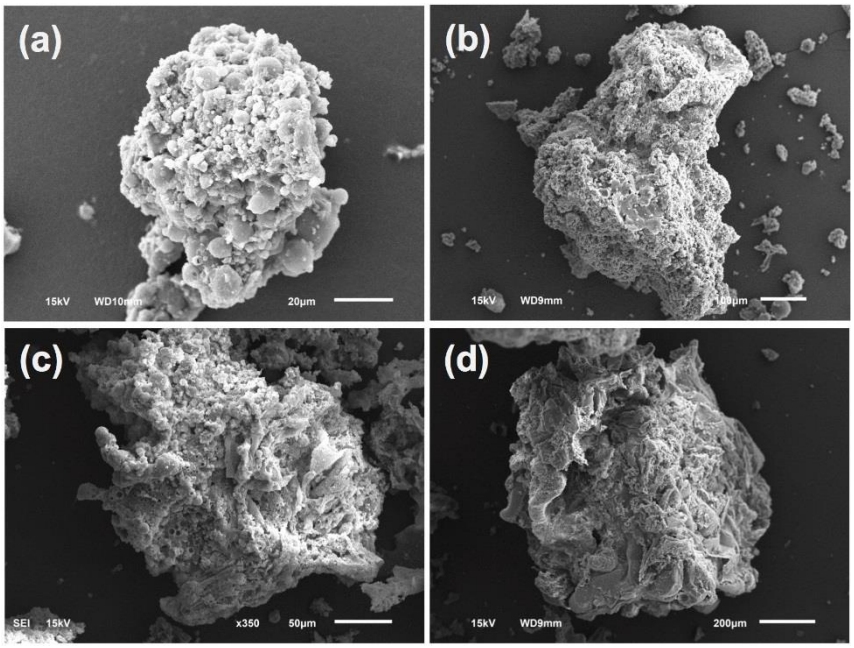

Figure 3.1: SEM images of (a) an inert PDMS bead containing no additives to the emulsion, (b) PDMS bead fabricated with $PtCl_4$, (c) $ZnCl_2$, and (d) NaCl introduced into the emulsion.

induce similar morphologies.[33] One such PDMS bead fabricated with $ZnCl_2$ in the aqueous phase of the emulsion is displayed in Figure 3.1(c). The spherical substructures are approximately the same size as the ones observed for samples created using $PtCl_4$, providing evidence of a high SAV ratio. The beads fabricated with $ZnCl_2$ are concave; traces of the metal ion were not found on the surface of the beads after rinsing.

The possibility of the ionic strength affecting the surface morphology was investigated by fabricating emulsions with sodium chloride (NaCl) dissolved in the aqueous phase. A representative SEM image of a PDMS bead fabricated with NaCl solution is depicted in Figure 3.1(d). Interestingly, the surface features observed are quite different from any other samples displayed in Figure 3.1. It is difficult to locate a spherical substructure that is observed for any other PDMS bead samples, while the

porosity is much less frequent. Qualitatively, this indicates that the ionic strength of the aqueous environment certainly influences the surface morphology, but not necessarily in such a way that would indicate an increase in the SAV ratio.

Brunaur-Emmett-Teller analysis was used to quantitatively assess the SAV ratio of each PDMS bead sample, the results of which are reported in Table 3.1. As predicted based on SEM images, $PtCl_4$ increases the SAV ratio over five times higher than pristine PDMS beads, but surprisingly, $ZnCl_2$ increases the amount of available surface area six times as high as platinum and approximately 30 times higher than the control procedure. The addition of NaCl, which is not expected to possess catalytic activity, resulted in a slight decrease in the SAV ratio compared to the control beads. This implies that, while a change in ionic strength certainly affects the physical features of the resulting PDMS beads, the primary factor in controlling the SAV ratio is the catalytic ability of the metal for the cross-linking of individual polymer strands.

The performance of a polymeric material for many other applications is dependent upon its SAV ratio, including its use a host material for photocatalysts. Due to their low density and inherent affinity towards nonpolar species in water, e.g. hydrocarbons found in petroleum-based fuel, the ability for PDMS beads to serve as a buoyant host material for photocatalyst particles was explored. Specifically, TiO_2 was anchored to PDMS beads and used to remove a model organic pollutant from aqueous solutions under exposure to UV light. The characterization and performance of these novel material are analyzed discussed in the remaining sections of this chapter.

Table 3.1: Surface-area-to-volume (SAV) ratios, determined by Brunauer–Emmett–Teller (BET) isotherm analysis, of the materials produced using aqueous phases with 0.012-M aqueous solutions of different electrolytes. First-column letters indicate the corresponding image panel in Figure 3.1. SAV ratios are based on the total surface area per unit mass, the mass of the sample, and the total cold free space of the sample.

Figure 3.1 Label	Salt Added	BET SAV Ratio (cm^2/cm^3)	SAV Improvement (relative to control)	Surface Density (m^2/g)
a	None (Control)	361.6	-	17.2
b	$PtCl_4$	1849	5.1	29.0
c	$ZnCl_2$	11060	30.6	64.9
d	NaCl	298.9	0.83	13.7

3.1.4 Incorporation of TiO_2

TiO_2 was chosen to serve as a model for photocatalyst incorporation because of its extensive availability, cost, and well-characterized photocatalytic properties.[9] To anchor the photocatalyst to the surface of the PDMS beads, nanofine TiO_2 powder (~21 nm diameter) was first dispersed in liquid PDMS. The same protocol was followed to fabricate PDMS beads, in that an emulsion was formed between water and the liquid polymer, followed by cross-linking, and eventual drop-curing in a heated water bath. As the PDMS chains are cross-linked and cured into a solid network, the photocatalyst particles became immobilized within and on the surface of the beads.

SEM images of beads created with and without TiO_2 are depicted in Figure 3.2. The pristine PDMS beads (Figure 3.2(a)) and ones inoculated with TiO_2 (Figure 3.2(b)) showed similar surface features, including convex morphologies, consistent with previous work.[33,34] This corroborates that the presence of nanometer-scale impurities does not affect emulsion formation drastically, indicating the PDMS beads still possess a high SAV ratio. Figure 3.2(c) and 3.2(d) depict close-up SEM images of select regions of the same pristine and TiO_2 inoculated PDMS beads. On the sub-micron level, rough surface features were visible which provide an appreciable amount of surface exposure for the anchored photocatalyst. It is evident that the morphologies on the submicron level are slightly affected, where less microspheres are seen in beads inoculated with TiO_2. Washing the beads in hexane, methanol, and water and performing sonication in water after fabrication did not remove appreciable amounts of TiO_2, suggesting that the photocatalyst is well-anchored to the buoyant host material.

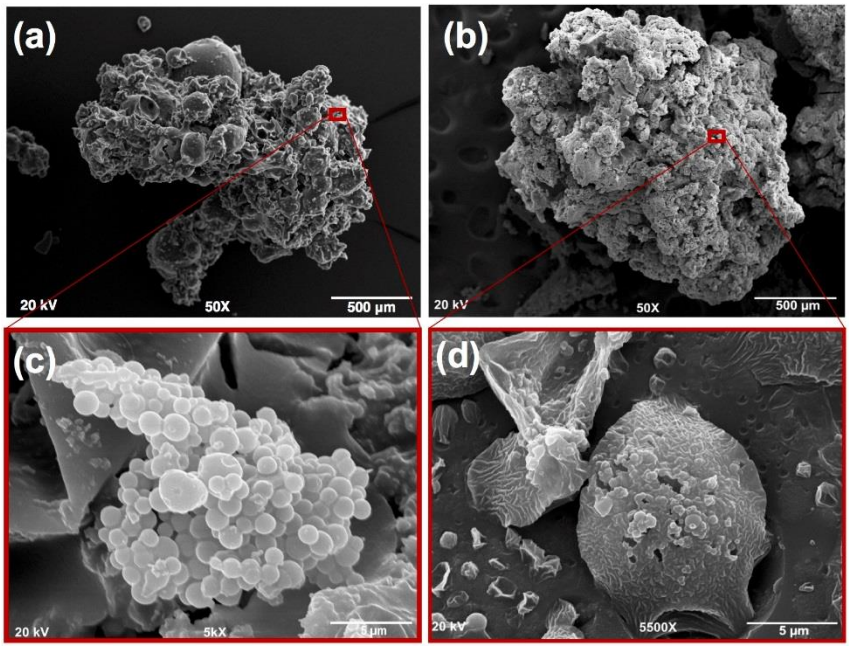

Figure 3.2: SEM images of (a) an inert PDMS bead and (b) a PDMS bead that has been inoculated with TiO_2. Zoomed regions of each image are indicated by the red squares and depict micro-morphologies consistent with proper emulsion formation for both (c) the inert PDMS bead and (d) the PDMS bead containing TiO_2.

3.1.5 Extent of TiO_2 Presence – Energy Dispersive Spectroscopy

An array of PDMS beads with varying loads of TiO_2 were fabricated to thoroughly assess the maximum host-capacity of the PDMS beads and to correlate photocatalytic performance to the amount of TiO_2 present. An amount of TiO_2 equivalent to 5%, 10%, and 20% photocatalyst-to-polymer mass ratio was dispersed in liquid PDMS prior to emulsion formation. To investigate the extent of TiO_2 inoculation in each sample, energy dispersive x-ray spectroscopy (EDS) was performed on the surface of several PDMS beads while in the SEM. Figure 3.3 depicts representative EDS spectra and corresponding SEM images of PDMS beads with 5% (a,b), 10% (c,d), and 20% (e,f) TiO_2 load are depicted.

The mass percent of Ti relative to Si elucidated from EDS data is reported in Table 3.2. This data suggests that the amount of photocatalyst present on the surface of the PDMS beads incrementally increases along with the amount of TiO_2 added to the emulsion. In the case of 0%, 5% and 10% TiO_2/PDMS loads, the runoff while washing the beads with various solvents was clear. However, with the 20% TiO_2/PDMS beads the runoff was a cloudy white solution characteristic of a TiO_2 suspension. This implies that a threshold for photocatalyst host-capacity has been reached for this method of fabrication, which is supported by the non-incremental increase in the Ti mass percent shown by EDS for the 10% and 20% loads. A 30% by mass TiO_2/PDMs mixture further decreases stability of the PDMS microspheres in water, preventing emulsion formation.

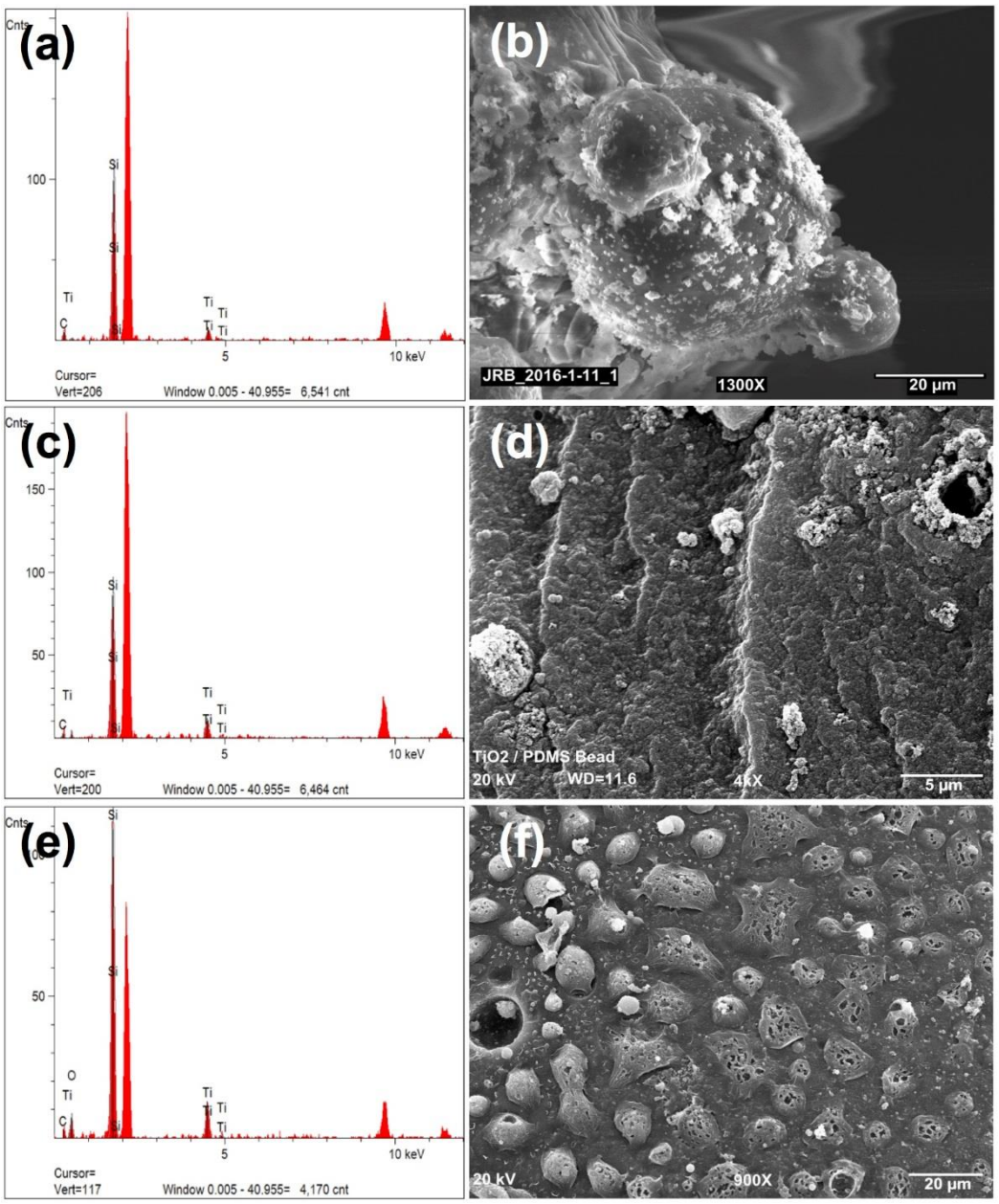

Figure 3.3: Energy dispersive spectra and corresponding surface SEM images for 5% (a, b) 10% (c, d) and 20% (e, f) TiO_2/PDMS loads used to assess the extent of photocatalyst load onto the buoyant substrate.

Table 3.2: Loading ratios and photocatalytic degradation rate constants for different beads produced in the study. Mass percent ratios (Mass % TiO_2) refer to the mass of TiO_2 added to the emulsion divided by the mass of the PDMS in the emulsion during synthesis. EDS Ti% is the mass percent of Ti relative to Si found using EDS analysis (the spectra and corresponding images are in Supplemental Information, Figure S-1). Rate constants (k_{TOT}, k'_{ads}, and k'_{hv}) are the slope of the natural log of absorbance of MB prior to equilibrium, relative to the initial absorbance. The pseudo-first order rate constants for adsorption (k'_{ads}) and photolysis (k'_{hv}), elucidated by control experiments, contribute to the total removal of MB (k_{TOT}). The pseudo-first order rate constant k'_{PO} represents MB removal only by photocatalytic degradation which is found by using the kinetic model developed in this work. The post-equilibrium total rate constant, k_{TOTeq}, is clearly consistent with the sum of k'_{hv} and k'_{PO}. Errors listed for rate constants are standard deviations, calculated from three trials; standard deviations for EDS Ti% were found by recording EDS spectra for three different beads for each respective load.

Mass %TiO_2	EDS Ti %	k_{TOT} (min^{-1})	k_{TOTeq} (min^{-1})	k'_{hv} (min^{-1})	k'_{ads} (min^{-1})	k'_{PO} (min^{-1})
0	0	-	-	0.0045 ± 0.0003	-	-
5	6.6 ± 0.8	0.008 ± 0.003		0.0045 ± 0.0003	0.0015 ± 0.0006	0.002 ± 0.003
10	11 ± 1	0.032 ± 0.003	0.013 ± 0.002	0.0045 ± 0.0003	0.018 ± 0.002	0.009 ± 0.004
20	15 ± 3	0.042 ± 0.002		0.0045 ± 0.0003	0.026 ± 0.001	0.012 ± 0.002
(TiO_2 Suspension)		0.36 ± 0.03	-	-	-	-

3.1.6 Raman Spectrum of TiO_2/PDMS Beads

It is known that TiO_2 undergoes a solid-state phase transition from the anatase crystal structure to its less photocatalytically active rutile crystal structure. Raman spectra of the TiO_2/PDMS beads were recorded to ensure that the method used to inoculate the PDMS beads and the extensive exposure to UV light during degradation trials does not affect the crystal structure. The conventional crystal cell of anatase TiO_2 is body centered. Six of its vibrational modes, $A_{1g} + 2B_{1g} + 3E_g$, are Raman active. The Raman spectrum of TiO_2 only, TiO_2/PDMS beads after synthesis, TiO_2/PDMS beads after three degradation trials, and inert PDMS beads are depicted in Figure 3.4. Frequencies of the Raman bands observed for TiO_2 are 398, 515, and 640 cm^{-1}. The band at 398 cm^{-1} is reportedly assigned to the B_{1g} vibrational mode of the anatase crystal structure.[87] The band at 515 cm^{-1} is reported to be a doublet of the A_{1g} and B_{1g} modes, while the band at 640 cm^{-1} is the degenerate E_g vibrational mode of the anatase crystal structure. The Raman spectra of TiO_2/PDMS beads before and after the degradation trials exhibit slight differences relative to the spectrum of TiO_2 alone. The band at 515 cm^{-1} appears to broaden slightly, and a new band emerges just above 700 cm^{-1}. To investigate this, the Raman spectrum of the solid PDMS beads was recorded as a reference. It appears that both the additional peak and the peak broadening observed for both TiO_2/PDMS spectra is due to the solid structure of PDMS. If rutile phase TiO_2 were present, bands would be expected to appear at 447 cm^{-1}, 612 cm^{-1}, and 827 cm^{-1} for the E_g, A_{1g}, and B_{2g} Raman active vibrational modes, respectively. Ultimately, the Raman spectra of TiO_2/PDMS beads before and after the degradation trials are nearly identical and possess all bands

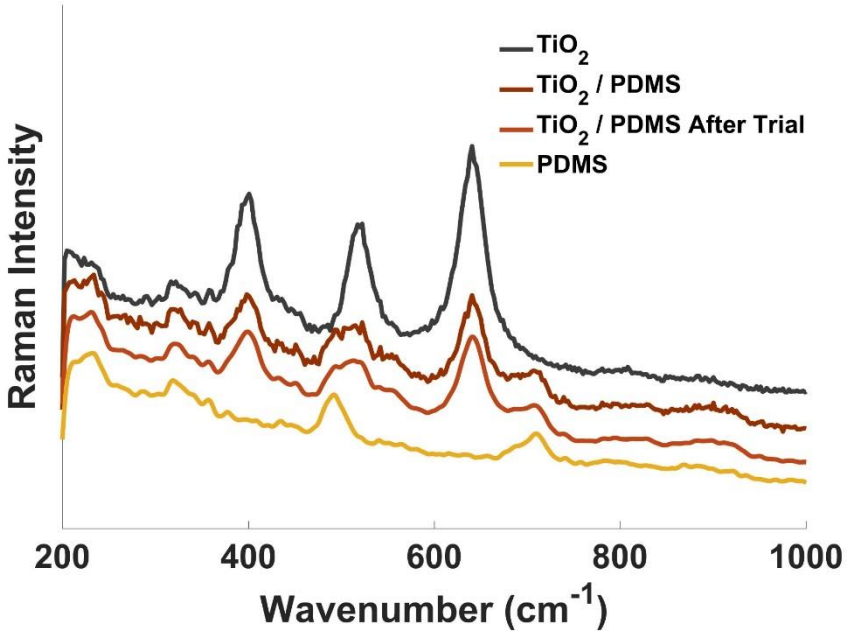

Figure 3.4: Raman spectrum of pure anatase TiO_2, TiO_2/PDMS after synthesis, TiO_2/PDMS after three consecutive 3‑hour long degradation trials, and inert PDMS beads.

observed for TiO_2 anatase, which indicates that neither the synthesis method, nor the degradation trials, alter the anatase crystal structure of TiO_2.

3.2 Degradation of Methylene Blue

This section details how pollutant removal performance of the TiO_2/PDMS beads was assessed using methylene blue (MB) as a degradation target. MB is a xanthene based dye (Chart 3.1) that is typically found in industrial waste streams.[88] It was chosen because it is a standard model pollutant for degradation experiments[8,25,27] and because its photocatalytic degradation process in the presence of TiO_2 is well‑characterized.[89]

3.2.1 Method of Analysis

As described in section 2.4.1, visible absorbance spectroscopy was used to directly assess the presence and relative amount of MB present in the aqueous solution as

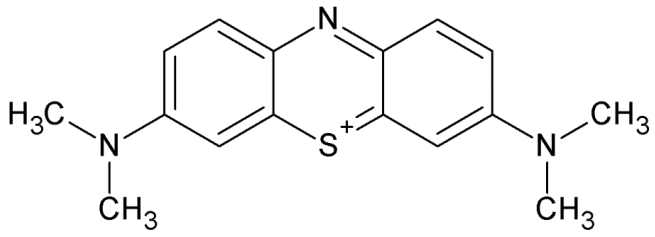

Chart 3.1: Molecular structure of the carcinogenic dye, methylene blue.

degradation experiments were performed. A typical set of MB spectra as a function of time under UV exposure while in the presence of 5% TiO_2/PDMS beads is shown in Figure 3.5. As the experiment progresses, the two peaks in the 550- to 750-nm range decay exponentially with time, as expected. The total peak area in this range is found by integration and used to assess the kinetics of MB removal. The inset of Figure 3.5 shows a plot of the natural log of the peak area ratio relative to the initial peak area prior to buoyant photocatalyst addition as a function of time. The strong linearity of this plot is consistent with the expected first-order degradation kinetics in MB: the negative slope for each experiment indicates the rate constant, k_{TOT}, for the removal of MB from solution.

3.2.2 Removal Performance and Langmuir Kinetics

Representative natural-log plots as a function of time are shown in Figure 3.6, with results summarized in Table 3.2. It is clear from the plot that k_{TOT} increases with photocatalyst load, as expected. All TiO_2/PDMS beads performed better at removal of MB from solution than inert PDMS or direct photolysis of MB without any additives. For trials containing 20% and 10% TiO_2/PDMS beads, the slope deviates from linearity at longer times, indicating an apparent change in rate constant at lower concentrations of

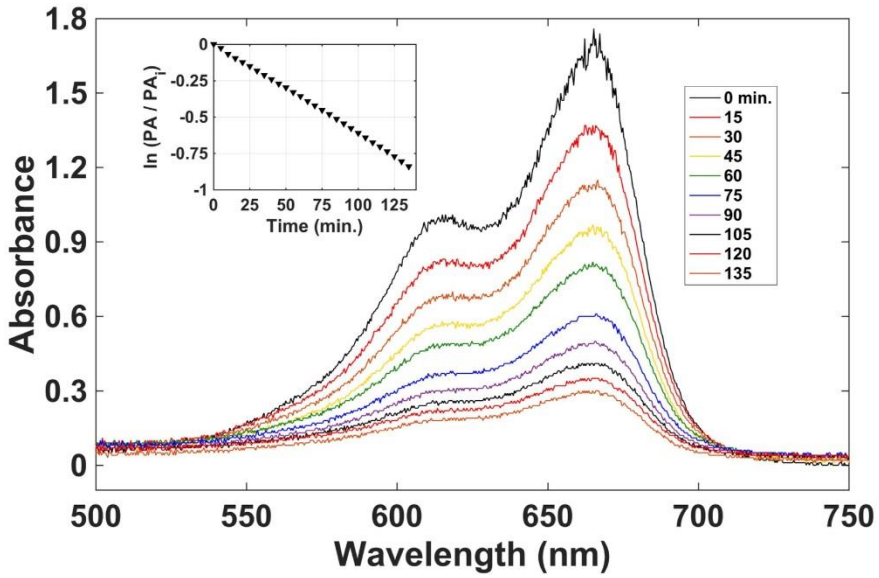

Figure 3.5: Visible absorption spectra of methylene blue recorded at consistent time intervals while being irradiated with UV‑Visible light in the presence of 5% TiO_2/PDMS beads. Inset plot shows the natural log of the peak area ratio as a function of time which suggests the removal rate of methylene blue is first‑order.

MB. It is known that Langmuir kinetics are observed in MB removal by adsorption onto TiO_2.[89] The equilibrium between the aqueous and adsorbed species results in a decreased removal rate by adsorption and an eventual cease of MB removal in the absence of light. In this work, adsorption equilibrium was not achieved prior to illumination under UV light, thus the decrease in the removal rate of MB observed near the end of the trials was attributed to the approaching adsorption equilibrium of MB onto the TiO_2 anchored to the PDMS beads. Therefore, the value of k_{TOT} for trials with 20% and 10% loads was determined from the first linear region of the natural log plots in Figure 3.6. An additional linear fit was applied to the second linear region for the higher loads and the negative slope calculated to isolate another rate constant, k_{TOTeq}, which is further

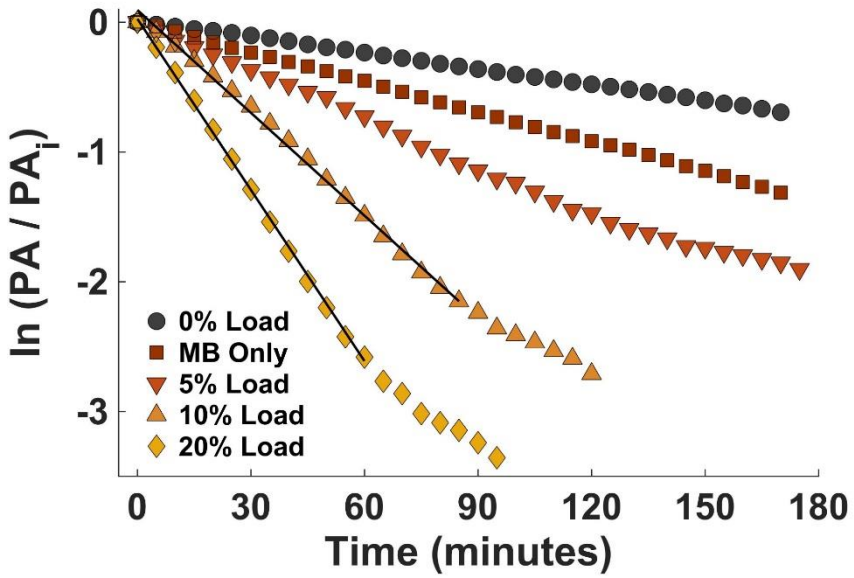

Figure 3.6: First-order kinetic plots (natural log of concentration relative to initial concentration) for MB solution using a series of beads with different TiO_2 loads. Also shown are inert PDMS beads (0% load) and photolysis of MB solution without any additives (Only MB). The slopes of the lines indicate the rate constant for loss of MB by adsorption, photolysis, and photocatalytic degradation. Two linear regions are observed for 20% and 10% loads due to MB adsorption equilibrium onto the beads resulting in a slight decrease in the removal rate; the value of k_{TOT} is based on the first region, indicated with a line in the plot.

discussed in Section 3.3.3. Results are presented in Table 3.2 and used to assess the validity of the kinetic model presented in Section 3.3.

3.3 Kinetic Model

Several phenomena contribute to the removal of MB from solution under UV light in the presence of the TiO_2/PDMS beads, including: (*i*) adsorption of MB, (*ii*) photolysis initiated by UV radiation striking the dye molecules, and (*iii*) degradation caused by photooxidative species generated by light-activation of the photocatalyst. Each can be accounted for using a series of control experiments. The contribution of MB adsorption onto TiO_2 to its removal from solution proved to be a non-negligible factor considering the decline of k_{TOT} observed in Figure 3.6 for the 10% and 20% TiO_2/PDMS

beads. Thus, the extent of MB adsorption and its contribution to the total amount of MB removed must be evaluated to assess the extent to which the photocatalyst is generating photooxidative species. Considering that the number of beads used does not completely cover the MB solution surface, direct photolysis (i.e., degradation by reaction of MB with radiation) could also play a major role. Most previously published photocatalysis results are unable to separate effects of direct photolysis and adsorption from true photocatalytic oxidation if experiments are performed in a turbid suspension of analyte and photocatalyst, unless those experiments also account for the opacity of the suspension, which has not been reported in the literature to date. This would necessarily involve parameterization based on the surface area and other details specific to a given experimental setup. To disentangle the various removal phenomena, a kinetic model is developed and presented in this section which serves to assess the extent of MB removal by attack of photooxidative species generated by light‐activation of the photocatalyst.

3.3.1 Presentation of Model Based on Removal Phenomena

Because there is no dispersed photocatalyst, and because the only objective is to monitor the degradation of MB, and not the generation of products, a kinetic model was used to disentangle the contributions of adsorption by using rate constant, k_{ads}, and direct photolysis rate constant, $k_{h\nu}$, from genuine photocatalytic degradation rate constant, k_{PO}, by oxidizers in solution, collectively $\{O_x\}$:

$$\begin{aligned} MB + TiO_2 &\xrightarrow{k_{ads}} MB@TiO_2 \\ MB + h\nu &\xrightarrow{k_{h\nu}} \{Products\}_{h\nu} \\ MB + \{Ox\} &\xrightarrow{k_{PO}} \{Products\}_{ox} \end{aligned} \qquad (3.1).$$

In this mechanism, each of the paths to removal of MB from solution (the experimental

observable) is first order in MB, and, given the very low concentrations of MB in solution, pseudo-first order overall, allowing the total reaction to be considered to have a single, pseudo first-order rate constant, k_{TOT}, which is the sum of the pseudo-first order rate constants for the three component reactions:

$$k_{TOT} = k_{ads}\left[TiO_2\right] + k_{h\nu}\left[h\nu\right] + k_{PO}\left[Ox\right] = k'_{ads} + k'_{h\nu} + k'_{PO} \quad (3.2).$$

To demonstrate the importance of adsorption of MB to TiO_2 and elucidate k'_{ads}, total absorbance measurements of MB solution are measured as a function of time following the addition of TiO_2 beads (with and without photocatalyst) to the solution while slowly stirring, but in a dark environment. Adsorption curves are shown in Figure 3.7. Like the anticipated degradation kinetics, adsorption appears to follow first-order kinetics. In all cases, the rate constants during irradiation are appreciably higher than (at least twice as high as) the dark experiments discussed in the previous section, indicating that, although some removal of MB from solution is due to adsorption directly onto the bead surface, photocatalytic degradation is also occurring. The extent of MB removed by direct photolysis, $k'_{h\nu}$, was measured by performing experiments with inert PDMS on the surface of the MB solution (0% TiO_2/PDMS load). This rate constant acted as a lower limit to MB removal in the presence of PDMS beads. Since these beads contained no photocatalyst, degradation of MB by photooxidative species is impossible. Also, because TiO_2 (not PDMS) is directly responsible for MB adsorption, photolysis must be the only phenomenon responsible for MB removal when inert PDMS beads are placed in the reaction vessel and subjected to degradation trials. Thus, $k'_{h\nu}$ solely represents the rate constant for the photolysis of MB in the presence of inert PDMS beads.

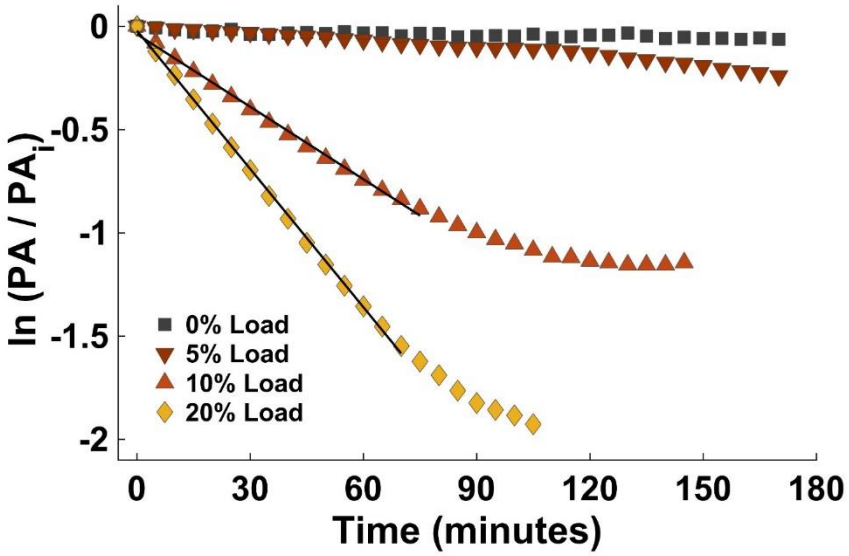

Figure 3.7: Adsorption curves for MB to TiO_2/PDMS beads. Visible absorbance spectra are collected in the absence of radiation capable of photolysis or photocatalytic activation to isolate the extent to which MB adsorbs to the beads as a function of time. Due to adsorption equilibrium, removal rates of MB for 10% and 20% loads began depreciating during the trial. Thus, the negative slope of the linear regions (indicated in the plot) are reported as k_{ads}.

3.3.2 Determination of Photooxidative Rate Constant

Assuming that [TiO_2] and [hv] are constant for all trials (for a given set of beads, the same amount of beads is used for each set of trials, and the lamp power is maintained at 300 W for all experiments), control experiments can be used to assess the first two terms in Eq. 2, thereby determining $k_{PO}[O_x]$ by subtraction based on the experimental values. These pseudo first-order rate constants, which are the best indicator of absolute photocatalytic degradation activity, are included in Table 3.2. Even when contributions from removal by adsorption and direct photolysis are considered, the pseudo-first order rate constant, k'_{PO}, for removal of MB by photocatalytic degradation is still found to account for a third of the total removal of MB for 5, 10, and 20% TiO_2/PDMS beads. As described in Section 2.4, the experimental design for testing MB degradation uses

top-irradiation, meaning that opacity of the beads would result in an expected lowering of the removal rate compared to MB solution without any beads, so this is a lower limit for removal by photocatalytic degradation. While adsorption complicates measurement of MB photocatalytic degradation, beads removed from the solution following complete degradation of the MB available in solution are white or light blue in color, while those recovered from the solution after the dark experiments were stained a deep blue. This indicates that degradation was occurring on the TiO_2 surface rather than only adsorption, in a period of approximately 50 minutes for the heavier loads of TiO_2. Thus, while adsorption contributes to the rate of MB removal slightly, it may also enhance the degradation by preconcentrating MB on the surface of the photocatalyst.

3.3.3 Validation of Model Using Langmuir Kinetics

To further assess the viability of this kinetic model, the rate constant k_{TOTeq}, (defined in Section 3.2.2) was elucidated from the negative slope of the second linear regions for the 20% and 10% load curves (Figure 3.5) as discussed in Section 3.2.2. The decrease in the removal rate observed relative to the initial linear region was attributed to an established equilibrium between species of MB adsorbed onto the TiO_2 surface and those remaining in solution. Thus, according to the kinetic model in Eq. 3.2, k_{TOTeq} should represent the removal of MB by photolysis and photooxidative species only. Indeed, the sum of k_{PO} and k_{hv} for 20% and 10% loads in Table 3.2 agrees with this kinetic model, with k_{TOTeq} values lying well within the reported uncertainties of the sum. This provides evidence that the kinetic model used to disentangle the various removal pathways of MB is valid. It provides a rate constant that solely represents the photocatalytic degradation of MB, which similar works are unable to do. Consistent use of this model in the future

could provide a means of normalizing how the performance of a buoyant photocatalyst is assessed and provide a means of direct comparison, provided that the degradation target is the same.

3.3.4 Reusability

To assess their viability for widespread application, buoyant photocatalyst materials should retain photocatalytic activity after several trials. The TiO_2/PDMS beads can be reused multiple times and still exhibit removal of MB by light-activation of the anchored photocatalyst. Second cycles of MB degradation trials were performed under the same experimental conditions, this time using beads that had been subjected to a single degradation period after washing with DI-water and hexanes. After the second cycle, these beads were gravity filtered, rinsed, and allowed to dry before submitting them to their third cycle of MB degradation. This process was repeated for the fourth and fifth trial. Figure 3.8 shows k'_{PO} for the same photocatalytic beads with varying TiO_2 load, each subjected to five consecutive degradation trials of MB. A slight increase in the rate constant was observed for the second trials for each TiO_2/PDMS load. This is attributed to minor contributions of adsorption of MB onto the photocatalyst. Although adsorption equilibrium is met within the first trial, as discussed in Section 3.2.2, washing the beads in various solvents prior to resubmitting them to degradation trials removes small amounts of adsorbed MB. Interestingly, k'_{PO} for the third trial of the 20% load drops below that of the 10% load, and it is acknowledged that this affect needs further investigation. Further consecutive trials display only minor fluctuations in k'_{PO}, indicating that the reusability of the TiO_2/PDMS beads as a buoyant photocatalyst is strong.

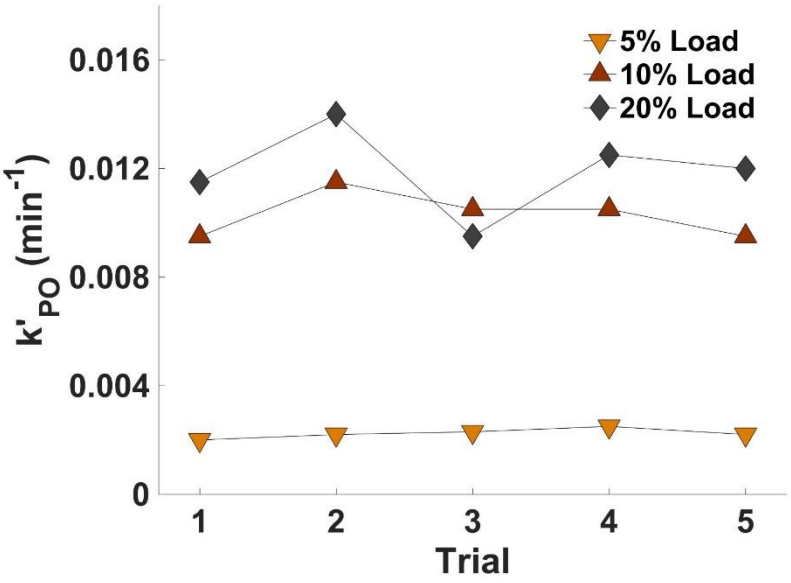

Figure 3.8: Reusability data for photocatalytic TiO_2/PDMS beads, showing k_{TOT} for three consecutive runs of 3 h each for each varying load of TiO_2.

3.4 Buoyant Photocatalyst Efficiency

It is difficult to compare the performance of different buoyant photocatalyst materials due to varying experimental parameters that affect degradation rates (such as light irradiation power, amount of buoyant photocatalyst used, concentration, and the identity of the model pollutant subjected to degradation). To compare effectiveness across analytical disparity in a uniform way, we have developed a parameter based on buoyant photocatalyst efficiency (BPE). This parameter, calculated according to

$$BPE = \frac{Pollutant\ Removed\ \ (mol)}{Light\ Source\ Power\ (W) \times Removal\ Time\ (min) \times Embedded\ Photocatalyst\ \ (g)} \quad (3.3),$$

depends on the amount of pollutant removed from water, and is inversely proportional to the power of the UV light source used in the experiment (assuming a Xe-arc lamp was used), to the amount of photocatalyst anchored on the buoyant support, and to the time

required to remove a particular number of moles of target species. Reports that assess materials based on the degradation of varying target species are not valid to compare by this method because their degradation pathways, thus their removal rates, will undoubtedly differ from one another.

3.4.1 Presentation of Equation and Dependencies

The available surface area of the materials, their average size, and the band gap of the photocatalyst will all impact a material's BPE because they are all inherent contributors to photooxidative effectiveness. Thus, BPE is designed to normalize experimental results based on controls and emphasize differences of photooxidative quality. Adsorption of the contaminants and the generation of radical oxidizing species ($OH\cdot$ and O_2^-) is highly dependent upon the amount of exposure that the photocatalyst has to the environment while being anchored to the buoyant support. Thus, an ideal support material should have a large amount of surface area to increase the number of adsorption sites and to increase the exposure of the photocatalyst to incident light, increasing the number of oxidative species generated. BPE also inherently compares the band gap of the photocatalyst, which dictates the total yield for the generation of oxidative species for a broadband source, such as sunlight, by affecting the fraction of radiation which can be converted to electron‑hole pairs. If the photocatalyst embedded in the buoyant support has a smaller band gap allowing visible light activation, then this material has a clear advantage over buoyant photocatalyst materials using UV‑restricted photocatalysts such as ZnO (3.3 eV)[90] and TiO2 (3.2 eV, anatase).[16] Thus, both the quality of the photocatalyst itself and the impact of the morphology of the substrate are measured by the BPE.

3.4.2 Comparison of TiO_2/PDMS Beads to Other Buoyant Photocatalysts

Table 3.3 compares the BPE calculated for various buoyant photocatalyst materials used in the degradation of MB found in the literature. Calculations from other work were made based on their reported values for the parameters used in Eq. 3. Of the previously reported works, the polystyrene sheets embedded with TiO_2[25] exhibit the lowest BPE by several orders of magnitude. This is likely due to the topology of the materials restricting the amount of available surface area, reducing the exposure of the loaded photocatalyst. The PDMS beads loaded with TiO_2 in this work produced a BPE much higher than the aforementioned materials, likely resulting from the discrete geometry and increased available surface area of the polymeric beads used as the host material. Free rotation of the beads at the surface of the interface (which cannot be accomplished with aerogels or slabs) could also be a significant advantage for pollutant environments, particularly those which are phase-separated. Notably, the BPE of the TiO_2/PDMS beads presented here rivals that of the fly ash cenospheres loaded with visible light active N-doped TiO_2 particles, which should have the advantage of a smaller band gap (2.7 eV).[91] The PS beads embedded with ZnO nanoparticles had the highest calculated BPE by two orders of magnitude.[8] It is known that ZnO outperforms TiO_2 in the degradation of MB in water[92] because it has a higher quantum efficiency for the degradation of organic pollutants.[93] However, ZnO is susceptible to photo-induced corrosion under acidic conditions,[94] hindering its reliability for commercial or large-scale environment applications. Regardless, our results suggest that PDMS beads outcompete other TiO_2-based buoyant photocatalysts, but that use of the same approach with better photocatalysts could yield even more impressive results. Additionally, the use of $ZnCl_2$ in

Table 3.3: Calculated buoyant photocatalyst efficiency (BPE) for various materials reported in the literature using MB as their degradation target.

Year	Material	BPE (mol W^{-1} min^{-1} g^{-1})	Reference
2016	TiO_2:PDMS Beads	4.1×10^{-4}	This work
2015	TiO_2:Polystyrene Sheet	2.5×10^{-6}	23
2015	ZnO:Polystyrene Beads	3.7×10^{-2}	8
2013	N-doped TiO_2:Fly Ash Cenospheres	4.4×10^{-4}	88

the aqueous phase of the emulsion would increase the SAV ratio of the buoyant substrate, which could result in a heightened amount of photooxidative species generated by the anchored photocatalyst.

3.5 Implementing Conductive Species in Poly(dimethylsiloxane) for Thermoelectric Applications

The band gap of PDMS is too large to conduct electricity, making it an insulator in the solid state. Thus, its ability to generate electricity from a temperature gradient as in a thermoelectric device would be expected to be low due to the large energy threshold. However, since PDMS has been reported to possess a low thermal conductivity (κ), it could serve as a host matrix for conductive species to prevent heat dissipation present in the conductive network by absorbing phonons. The following sections detail the cross-linking of two conductive organosiloxane molecules into separate regions of PDMS to create a bulk heterojuction (*p*-*n*) on the microscale for use as a thermoelectric material. This regioselectivity is made possible by cross-linking these species in the presence of an emulsion.

3.5.1 Cross-linking Rhodamine-B Silane and Anthracene Polyhedral Oligomeric Silsesquioxane into PDMS Beads

Two organosiloxane species are cross-linked into PDMS to create a bulk heterojunction on the micro-scale, whose structures are depicted in Chart 3.2. Rhodamine-B Silane (RBS) is a derivative of the common dye rhodamine-B possessing a carboxamide linker with a three-carbon chain attaching a triethoxysilane tail with an Si – C bond (Chart 3.2(a)). The other conductive species (Chart 3.2(b)) is a cage-like molecule termed polyhedral oligomeric silsesquioxane with an anthracene attached as a functional group (POSS-ANT). RBS was found to be an *n*-type semiconductor[79] while POSS-ANT is a *p*-type.[80]

RBS is a cation chloride species, dissolving readily in water while remaining insoluble in aliphatic solvents such as *n*-heptane, while the opposite is true for POSS-ANT because it is largely nonpolar. Thus, when an emulsion is formed with RBS in the continuous, aqueous phase and POSS-ANT in the discrete, largely nonpolar phase, the conductive species will appear in separate regions of the beads' microstructure upon heat-curing. Due to their opposing majority charge carriers, this could create a *p*-*n* junction on the microscale, with RBS in the outer regions of PDMS (where the aqueous phase was present) and POSS-ANT being embedded within the polymer. Because of their organosiloxane components and the reliance of the PDMS cross-linking mechanism on Si – O bonds, their implementation into PDMS beads by simple solvation into the emulsion would result in an electrically conductive network within the solid polymer matrix if sufficient amounts of both species are implemented into the solid network.

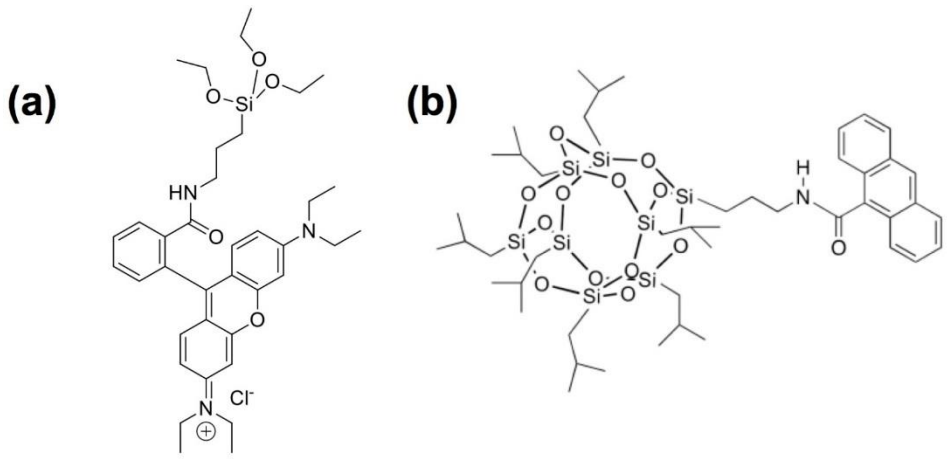

Chart 3.2: Molecular structures of (a) RBS and (b) POSS‑ANT.

3.5.2 Characterization and Performance

An image of a representative PDMS bead with both conductive species implemented into its matrix can be seen in Figure 3.9(a). Overall, the beads were rather large compared to ones discussed in previous sections, possessing a diameter of a few millimeters. Thus, their morphology could be inspected using a light microscope. The general structure of the bead is the same, possessing a convex porosity composed of agglomerated PDMS spheres indicating that the two additives do not affect emulsion formation. The beads are stained a pink‑orange color resulting from addition of the RBS dye.

RBS and POSS‑ANT are both highly fluorescent compounds: both experience excitation in the UV range (~340 nm), but emit at very distinct wavelengths, 610 nm and 420 nm, respectively. Therefore, the location of each conductive species within the PDMS becomes apparent when illuminated with UV radiation fluorescence is observed. To accomplish this, a 340 nm band pass filter was placed in front of a Hg EXFO light and directed onto the PDMS bead under a light microscope. With no additional lighting, it

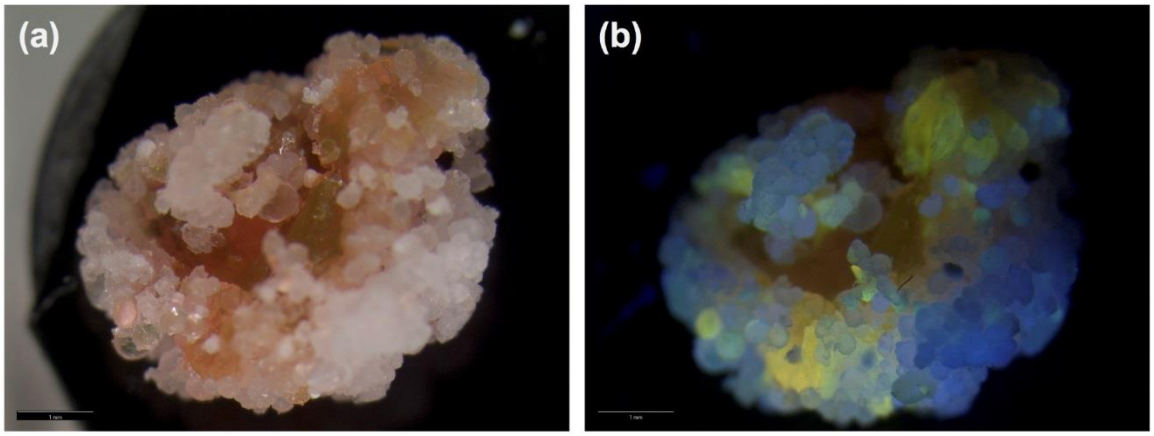

Figure 3.9: Light-microscope image of PDMS bead cross-linked in the presence of rhodamine-B silane and polyhedral oligomeric silsesquioxane anthracene. The emission is fueled by a UV light with a 340 nm band pass filter illuminating the fluorescent bead at a 90° angle. The blue fluorescence is due to anthracene, while the orange fluorescence is attributed to rhodamine-B.

was possible to capture an image of the fluorescent bead, which is depicted in Figure 3.9(b). There appear to be two distinct regions of color within the PDMS bead. The orange-yellow region located within the beads infrastructure is attributed to RBS whose emission wavelength is in the appropriate region of the visible spectrum. The blue spheres located towards the exterior of the bead's structure are filled with POSS-ANT. The separation between the two conductive species showed great promise that a bulk *p*-*n* junction on the microscale within the PDMS beads had been created.

After this discovery, thermoelectric characterization of this material began. Many approaches were taken to elucidate the electrical conductivity, but subjecting these materials in any form to an applied voltage resulted in a negligible amount of current. Two possible reasons that explain the lack of conductivity. Because these two species conduct opposing charge carriers and are so closely implemented in the same structure, there could be electron-hole recombination within the structure of PDMS before the

charge carriers reach the electrodes. Alternatively, the agglomeration of PDMS spheres causes many discontinuities within the solid matrix, inhibiting the direct flow of charge carriers to exterior electrodes. Although these materials could not be used for thermoelectric applications, the concept of creating a bulk heterojunction on a microscale by using emulsion morphologies has been proven possible by this work and could be extended to other thermoelectric systems to boost power output.

CHAPTER IV

Copper (II) and Rhodamine-B Silane Results and Discussion

Further studies using PDMS as a host-matrix for thermoelectric applications were postponed to properly characterize the thermoelectric properties of the novel organosiloxane compound, RBS. To our knowledge, RB nor any of its derivatives had been subjected to thermoelectric characterization prior to this study. The thermoelectric properties of RBS as a thin film are presented in this chapter, and proved to be rather low compared to other organic semiconductors. However, derivatives of RB have shown enhanced electronic properties upon coordination to a transition metal ion, specifically Cu^{2+}. Thus, studies were then focused on the coordination of RBS to Cu^{2+} (Cu-RBS) with intentions of forming an organic/inorganic hybrid system to boost thermoelectric performance. This chapter details the results of the characterization of the novel complex Cu-RBS, and begins with computational simulations.

4.1 Computational Simulations

Density functional theory (DFT) calculations were used to provide insight into the enhanced photophysical properties and thermoelectric performance of rhodamine-B silane (RBS) observed upon complexation to Cu^{2+}. The B3LYP[83] DFT method and the 6-31G[84] split-valence basis set were applied to all calculations, except those involving a Cu^{2+} ion. In those cases, a split-basis set calculation was used to apply the LANL2DZ[85] pseudo-potential basis set to copper ions, while 6-31G was maintained for all other atoms. Many aspects of the theoretical simulations were analyzed including (*i*) favorable Cu^{2+} positions in proximity to RBS, (*ii*) electrostatic potential (ESP) surfaces, (*iii*) torsion

angles of crucial conjugated moieties of the chromophores RB and RBS, (*iv*) dipole moments, (*v*) lowest energy electronic transitions, and (*vi*) molecular orbital contours. Prior to presentation of experimental results, the results from the copper ion position optimization search and the generated ESPs are first discussed in the following subsection to provide the reader with a sense of identity for the new complex. The latter aspects of the computational simulations mentioned are presented along with experimental results discussed in later sections for direct comparison.

4.1.1 Optimal Position of Cu^{2+} Proximal to Rhodamine-B Silane

To find the most energetically favorable position of Cu^{2+} relative to RB and RBS, many separate geometry optimization calculations were performed with the metal ion starting in different locations for both molecules using B3LYP/6-31G method and basis set, while LANL2DZ basis set was applied only to Cu^{2+} atoms. Initial positions of the metal ion for RB were chosen based on the electrostatic potential (ESP) surface generated for the optimized structure of RB by Mulliken population analysis[95] in GaussView, which is depicted in Figure 2.2(a). Much of the electron density was concentrated near the outer regions of the molecule, resulting from the electronegative atoms (N and O) located in these regions. A metal cation such as Cu^{2+} may prefer these sites due to the less positive potential in this region. Despite its more positive potential, the xanthene core of RB is regarded as a potential metal binding site because of its conjugated structure. The sp^2 hybridized C atoms possess un-hybridized *p*-orbitals, which can bind to a metal atom's *d*-orbitals if they are close in energy and possess the necessary symmetry that allows their orbitals to overlap, according to ligand field theory.[96]

The ten copper ion placements chosen for RB are presented in Figure 2.2(b). Geometry optimization calculations using DFT were performed for each position, and the results of each in terms of relative energies are reported in Table 4.1. Position 10 was found to be the optimum with the spatially equivalent position 9 with a nearly negligible difference in ΔE compared to other positions. In fact, positions 3 and 4, 5 and 6, and 7 and 8 are spatially equivalent, thus it is not surprising that their energies are the same. It is worth mentioning that all calculations performed with a copper ion placed on the face of RB opposite to the carboxylic acid group (positions 1, 2, 7, and 8) were significantly higher in energy than any other positions. This suggests that the metal ion favors the side of RB with the carboxylic acid group, likely because of its higher electron density in this region.

The ESP for RBS (Figure 2.3(a)), along with the results from copper ion placement around RB, provided several promising copper ion positions around the silanized rhodamine derivative. The ESP for RBS, compared to RB, exhibited a large shift of electron density down from the xanthene core to the O of the carboxamide linker and silane tail. This introduces new energetically favorable positions for the metal ion that are not possible for RB. Based on both the ESP of RBS and the most energetically favorable positions of Cu^{2+} around RB, copper ions were placed in seven different positions around RBS (Figure 2.3(b)) and subject to geometry optimization calculations. The results for this series of calculations are reported in Table 4.1. Position 6 was found to be the most energetically favorable location for the metal ion, which is in proximity to the N of the carboxamide group and an O of the silane tail. Position 1, which corresponds to a copper ion placement near the xanthene core of RBS, was much higher in energy

Table 4.1: Relative energies of geometry optimization calculations performed with Cu^{2+} in various positions around RB and RBS used to find the most energetically favorable position for the metal ion.

Position	ΔE (eV)	
	Cu^{2+} and RB	Cu^{2+} and RBS
1	0.88	0.87
2	1.59	1.40
3	0.17	1.60
4	0.17	2.13
5	0.55	2.80
6	0.55	0
7	1.07	1.20
8	1.07	
9	0.9×10^{-8}	
10	0	

relative to the optimum, with a ΔE of 0.87 eV. This indicates that the addition of the silane tail to the rhodamine moiety introduces new, more energetically favorable positions for which metal ions can come near the chromophore, possibly enabling participation in charge-transfer.

The optimal arrangement of Cu^{2+} and RBS is depicted in Figure 4.1. This species will be further referred to as copper rhodamine-B silane (Cu-RBS). Placement of the metal ion in this position causes the 3-carbon chain connecting the carboxamide group and the silane portion to curve away from Cu^{2+}, allowing an O atom to secure the metal ion between it and the N atom. The distances between N-Cu^{2+} and O-Cu^{2+} are 1.92 Å and 1.90 Å, respectively, where the small difference was attributed to the electronegativity of the O atom. This coordination site has important implications on the electronic structure, and therefore electronic properties, of the chromophore RBS because

conjugation throughout the entire molecule is made possible by metal ion complexation at this specific site. Normally, the silane tail of RBS alone does not participate in conjugation because of the saturated 3-carbon chain linker to the RB moiety. However, when the metal ion is introduced, a conjugation pathway is provided from the silane tail directly to the carboxamide linker, bypassing the sp^3 hybridized carbon chain. This provided initial evidence that RBS acts as a Schiff-base ligand,[76,77] forming a metal/organic coordination complex with Cu^{2+}. The metal ion acts as a Lewis acid, accepting lone pair electrons from the N of the carboxamide group and an O of the silane tail. Many similar Schiff-base systems have been identified according to literature (as detailed in Section 1.4.2), and have exhibited an enhancement in electronic properties upon complexation that can be observed in solution by UV-visible absorption and fluorescence emission spectroscopy.

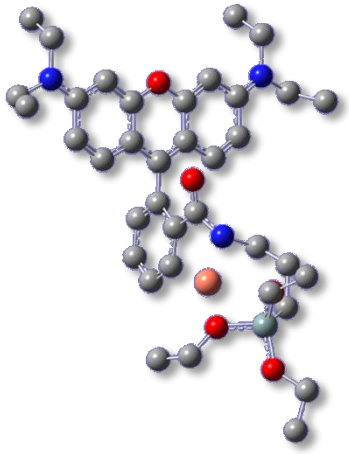

Figure 4.1: Optimal geometry of Cu-RBS predicted by B3LYP/6-31G /LANL2DZ imaged in GaussView. Cu is orange atom.

4.2 Photophysical Properties in Solution

Schiff-base systems involving UV-visible active species have been shown to exhibit alterations in their photophysical properties upon complexation. Therefore, the fluorescence emission and UV-visible absorption spectra of RBS and Cu-RBS were recorded, while RB and Cu-RB were used as controls. The results from these experiments are discussed in this section, and supported with frontier molecular orbital contours and their energies provided by computational simulations.

4.2.1 Fluorescence Emission Spectra

To provide additional insight into effects of the interactions between Cu^{2+} and the rhodamine derivative, fluorescence emission spectra of RB, RBS, Cu-RB, and Cu-RBS as well as RBS with varying Cu^{2+} mol% (Figure 4.2) were recorded. Figure 4.2(a) depicts the vibronic emission spectrum of RBS with Cu^{2+} concentration increasing steadily from 0:1 to 1:1 mole ratio of Cu^{2+} to RBS. With each incremental increase in metal ion concentration, the fluorescence emission intensity of RBS increases at a consistent rate. For comparison purposes, Figure 4.2(b) depicts the fluorescence emission measurements of RB, RBS, and Cu-RB compared to Cu-RBS at equal molar concentrations. Cu-RBS is the only species that experiences an increase in fluorescence emission. This indicates that coordination of the metal ion to RBS is stable and enhances the vibronic transitions, while the same may not be true for Cu-RB. These observations provided further supporting evidence that RBS acts as a Schiff-base ligand for Cu^{2+}, as predicted by the optimal position of the metal ion in the computational simulations. The increase in fluorescence observed for the Cu-RBS complex is consistent with reports in the literature

in which Schiff-base RB derivatives were used to pinpoint the locations of Cu^{2+} ions in various biological environments by an increased fluorescent emission.[76,77] In these reports, the fluorescence increase is attributed to a spirolactam (ring-opening) mechanism of the RB derivative initiated by the presence of a metal ion. These spirocyclic (ring-closed) forms have a low quantum efficiency, but when converted to its spirolactam form show increases in both absorbance and fluorescence emission intensity. In fact, RB itself is known to possess an equilibrium between these two forms in solution.[97]

The molecular structure of RBS is similar to other RB-based Schiff-bases, which all possess an amide group attached to the lone benzene in the ortho position that is known to participate in conversion from the spirocyclic to the spirolactam form. The predicted mechanism of the RBS spirolactam ring-opening induced by the coordination of RBS and Cu^{2+} is displayed in Scheme 4.1. The optimal configuration of Cu-RBS predicted by computational simulations described in Section 4.1.1 indicated that the most energetically favorable Cu^{2+} position is between the N of the carboxamide group and an O of the silane tail. Thus, the metal ion prevents formation of the spirolactam form of RBS in solution, increasing the fluorescence emission intensity of the chromophore. RB solutions with Cu^{2+} do not experience this phenomenon because the most energetically favorable metal ion binding site is not close enough to the carboxyl group to prevent spirocyclic formation of the chromophore in solution.

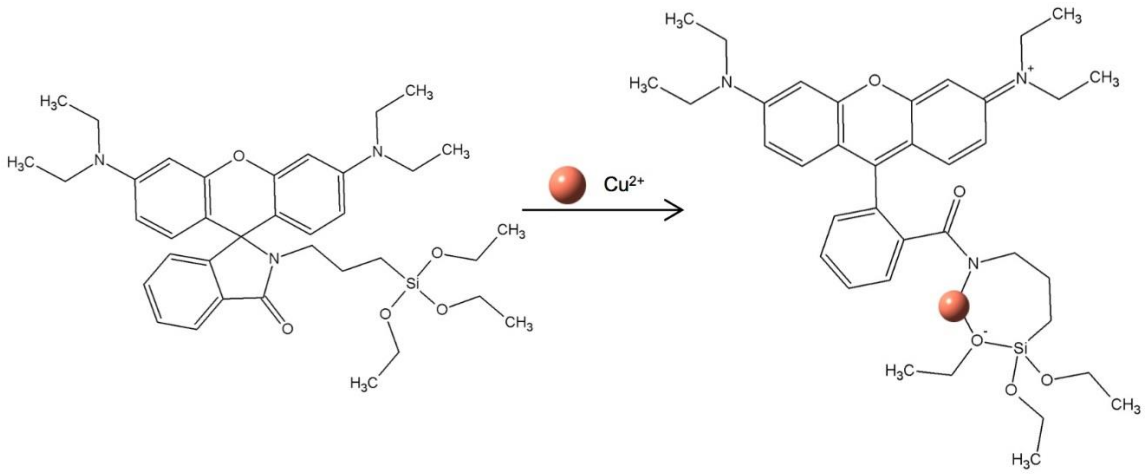

Scheme 4.1: Depiction of RBS converting from its visibly inactive spirocyclic form to its visibly active spirolactam form upon coordination to Cu^{2+}.

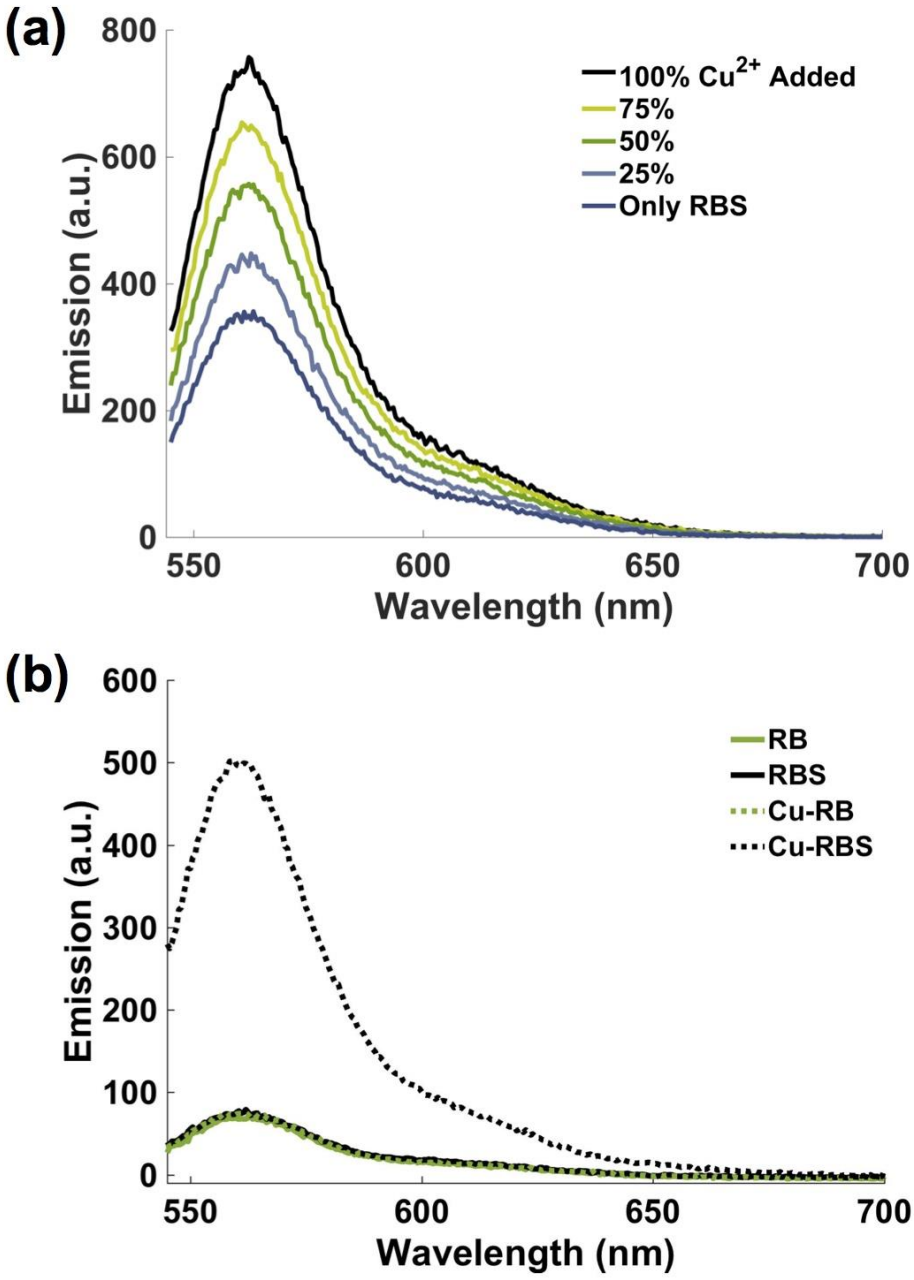

Figure 4.2: Fluorescence emission measurements in 2−propanol of (a) RBS with increasing mol % of Cu^{2+} and (b) RBS along with RB, Cu‑RB, and Cu‑RBS.

4.2.2 Solution-based UV-Visible Absorption Spectral Characteristics

A series of absorption measurements were carried out for RB, RBS, Cu-RB, and Cu-RBS in 2-propanol to provide further insight into the interactions between Cu^{2+} and RBS. The solution phase visible absorption spectrum for each species at a chromophore and Cu^{2+} concentration of 9 μM (1:1 chromophore-metal mole ratio) is shown in Figure 4.3(a). All solutions exhibit similar peak positions; possessing a main absorption peak centered near 540 nm. This main absorption peak results from the $\pi \rightarrow \pi^*$ electronic transition within the chromophore.[76] The absorption magnitude of Cu-RB and Cu-RBS is nearly twice that of the metal ion-free solutions.

Additional absorption measurements were conducted in solution to provide more insight into the possibility of an energy transfer between Cu^{2+} and RBS. The absorption of RBS at a fixed concentration while increasing the concentration of Cu^{2+} in increments is shown in Figure 4.3(b). Absorbance intensities of the chromophore gradually increase as Cu^{2+} concentration increases by 25, 50, 75, and 100 mol%. Ultimately, a three-fold increase in the absorbance intensity was observed transitioning from a Cu^{2+} concentration to a 1:1 mole ratio with RBS. Two explanations for this occurrence are possible. First, the presence of the Cu^{2+} ion could shift the spirolactam/spirocyclic equilibrium, favoring the visible-light active ring-open form of RBS, and thus, allowing a larger population of the chromophore to absorb photons of the appropriate wavelength. However, this does not explain the increase in absorbance observed for Cu-RB since fluorescence data provided evidence that Cu^{2+} does not convert a significant population of RB molecules into its spirolactam form. Alternatively, Cu^{2+} possesses a highest occupied molecular orbital

(HOMO) very near the HOMO of RB and RBS, allowing a charge transfer to take place between the organic and metal ion species.

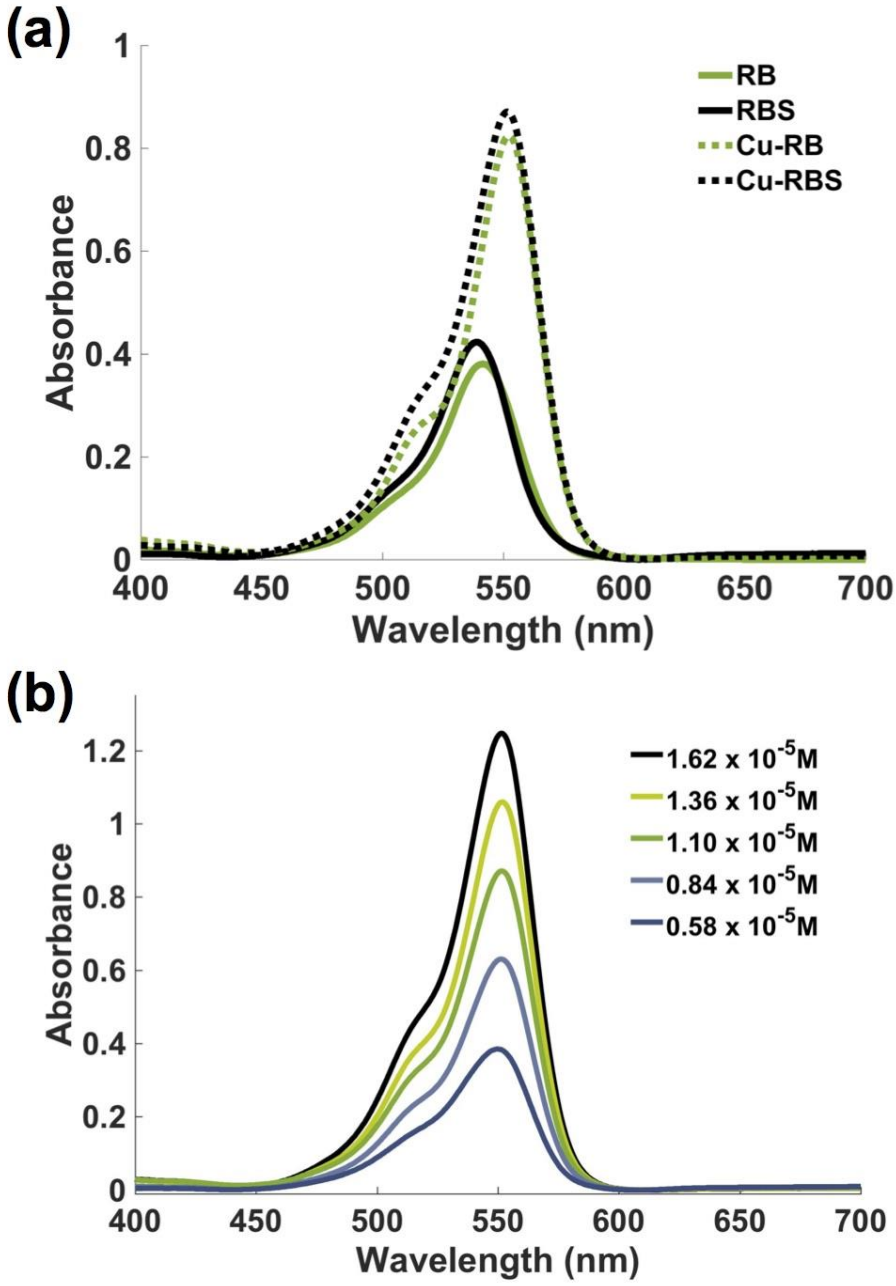

Figure 4.3: UV‑visible absorption measurements of (a) RB, RBS, Cu‑RB, and Cu‑RBS at equal molar concentration, and (b) RBS with increasing molar concentration of Cu^{2+}.

4.2.3 Theoretical Molecular Orbital Distributions

To investigate that possibility that Cu^{2+} and RBS are participating in a charge transfer, theoretical contours of the occupied and unoccupied molecular orbitals of RB, RBS, Cu-RB, and Cu-RBS were obtained using the same method and basis set combination used for geometry optimization calculations and visualized in GaussView.[82] The spatial distributions of the highest occupied molecular orbitals (HOMO) and lowest unoccupied molecular orbitals (LUMO) predicted for RB and RBS are shown in Figure 4.4. For both species, the lowest energy electronic transition was isolated on the xanthene structure of the chromophore. Because of the doublet spin-multiplicity, calculations involving the open-shell Cu-RB species produced two sets of singly occupied molecular orbitals (SOMOs) for the alpha- and beta-spin (α- and β-spin) electrons.

Contours of select energy levels for Cu-RB are depicted in Figure 4.5. Both the highest occupied SOMOs and lowest occupied SOMOs possessed minor contributions

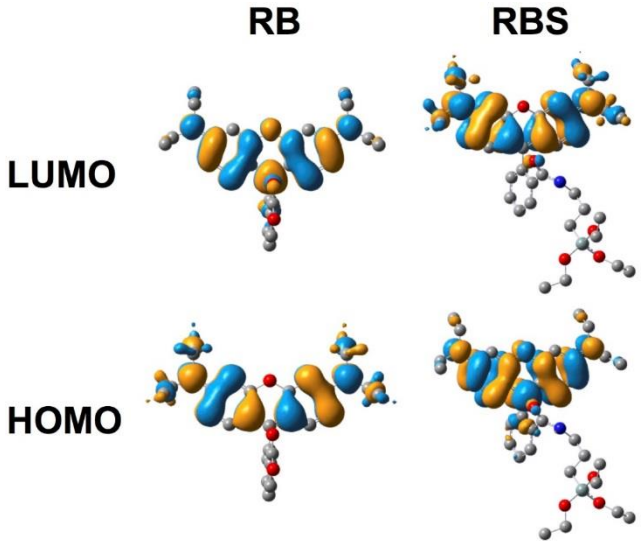

Figure 4.4: Molecular orbital contours of the HOMO and LUMO energy levels for RB and RBS.

from *d*-orbitals of the copper ion located next to RB. Both orbitals are located primarily on the xanthene core of RB, indicating that a charge transfer does not occur. However, contribution from the metal ion to these sets of molecular orbitals may serve to increase the population of excitable electrons upon absorption of a photon, thus elucidating the enhanced absorption properties observed for Cu-RB in solution. The lower lying occupied SOMOs (HOMO-1, and HOMO-2) of Cu-RB are more than 0.6 eV lower in energy than the HOMOs, indicating that electrons located in these orbitals require significantly more energy to be excited to the LUMO level than electrons located in the HOMO.

Some contours of the molecular orbitals and their energy levels for Cu-RBS are shown in Figure 4.6. Despite spin-contamination, the contours of both α- and β-spin orbitals provided by DFT displayed multiple metal-to-ligand charge transfers (MLCT) that occur for the low-energy electronic transitions. This is demonstrated by the contours in Figure 4.6. The highest occupied SOMOs possess d_z^2 character from Cu^{2+}, while the lowest unoccupied SOMOs are located on the xanthene core of RBS. Surprisingly, the second HOMO (HOMO-1) of Cu-RBS for both α- and β-spin orbitals also possess metal ion character, depicting contributions from the d_{yz} or d_{xz} orbitals of Cu^{2+}. The contours of the third HOMO (HOMO-2) of Cu-RBS resembled those of the HOMO of all other species, where the electron density was located on the xanthene core. Comparing the energetic locations of these energy levels; there was a relatively small energy difference between the HOMO, HOMO-1, and HOMO-2.

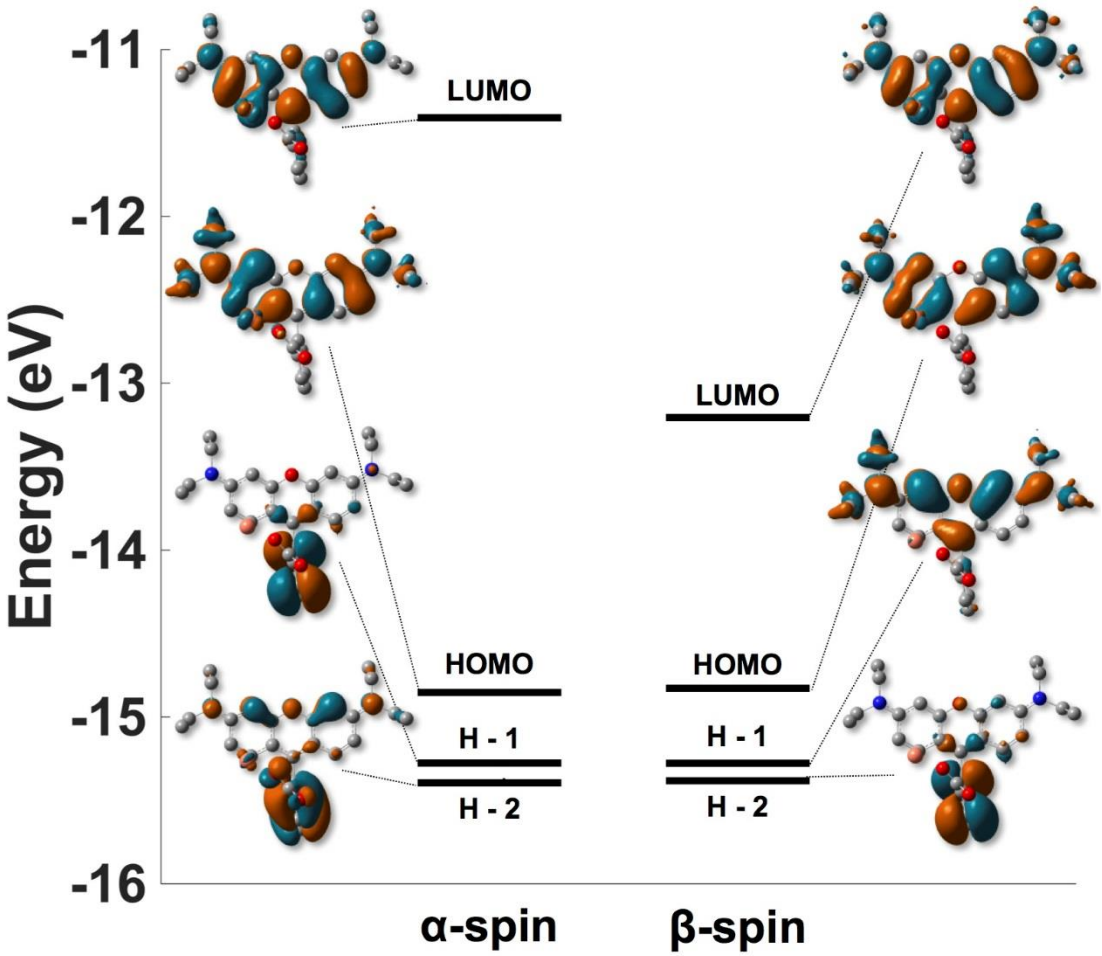

Figure 4.5: Molecular orbital contours and relative energy levels for Cu‑RB including the LUMO, HOMO, HOMO – 1, and HOMO – 2 for both α‑ and β‑spin configurations.

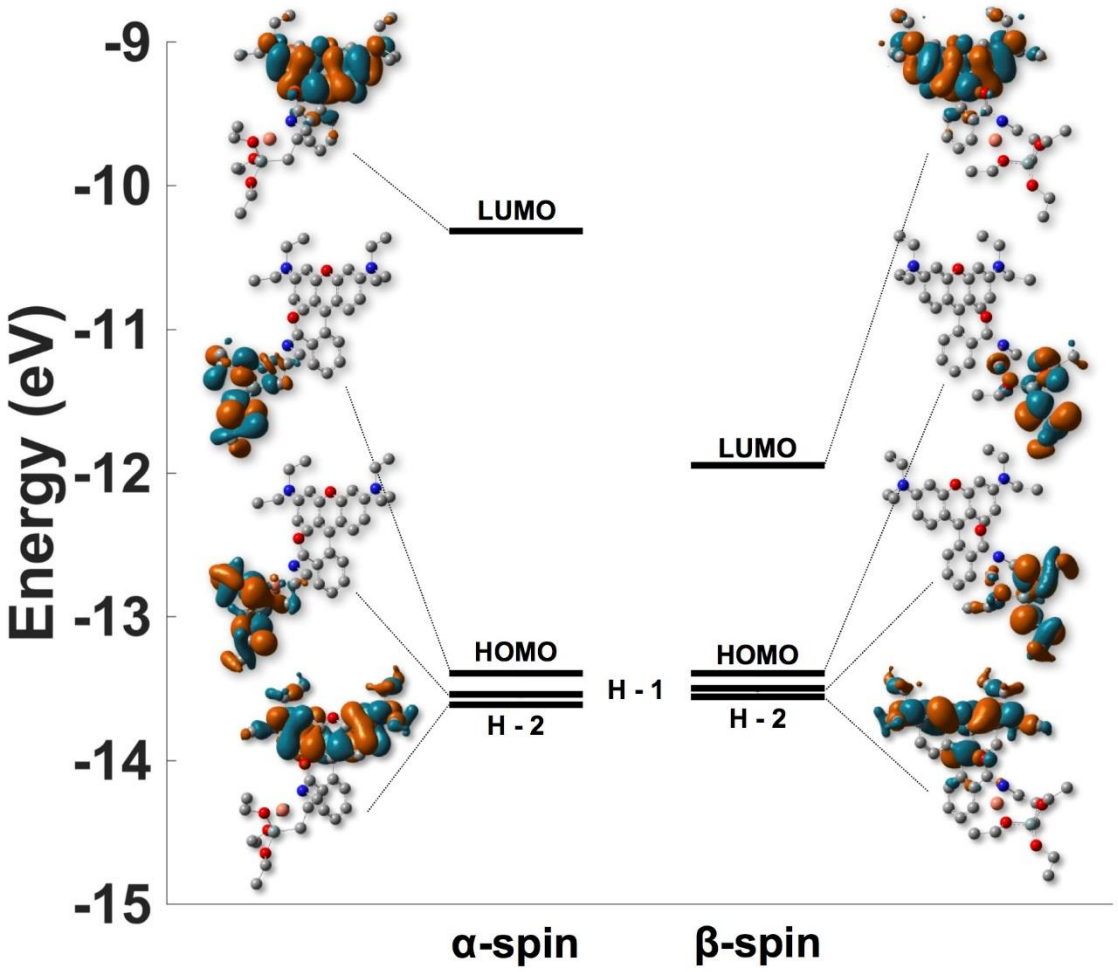

Figure 4.6: Molecular orbital contours and relative energy levels for Cu‑RBS including the LUMO, HOMO, HOMO – 1, and HOMO – 2 for both α‑ and β‑spin configurations.

Reports have shown that Cu^{2+} readily assumes a square planar coordination geometry when attached to polydentate ligands.[98,99] Many inorganic chemistry textbooks presenting crystal field theory[100] depict the valence *d*-orbitals of a square planar coordination geometry metal ion like the one depicted in Figure 4.7 for a d^9 electron configuration.[101] According to the Jahn-Teller theorem,[102] the *d*-orbitals of a coordinate metal ion will distort (lower its symmetry) to remove degeneracy, avoiding electronic configurations that are energetically unfavorable. The lowest energy levels of the square planar geometry are predicted to be composed of d_{yz}, d_{xz}, and d_z^2 orbitals. *d*-orbitals with the same symmetry were observed to contribute to the HOMO and HOMO-1 of Cu-RBS, implying that coordination of Cu^{2+} introduced two new occupied energy levels just above the original HOMO of RBS that can take place in MLCT transitions. This is only accessible to RBS, and not RB, because silanization allows RBS to act as a Schiff-base ligand. These theoretical results, along with the observed increase in fluorescence emission and absorbance, indicate that not only is Cu^{2+} inhibiting formation of the spirocyclic form of RBS, but is also participating in multiple MLCTs, resulting in a drastic increase of both fluorescence emission and visible absorption in solution.

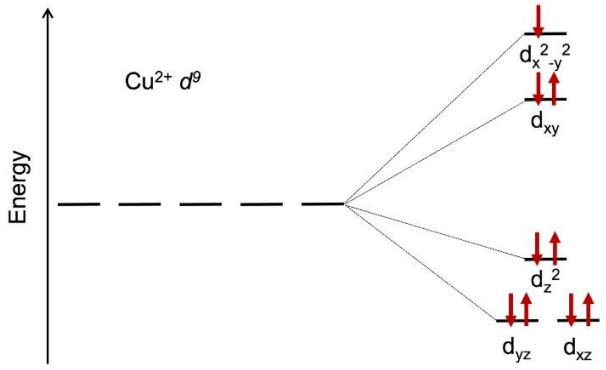

Figure 4.7: Depiction of the Jahn-Teller distortion effect on the *d*-orbitals for a square planar geometry metal ion with a d^9 valence configuration.

4.3 HOMO-LUMO Energy Gaps

HOMO-LUMO energy gaps provide mechanistic insight into alterations in electronic properties of materials in the solid-state. In this section, the HOMO-LUMO energy gap is determined for RB, RBS, Cu-RB, and Cu-RBS by solid-state absorption spectroscopy and theoretical methods. Results from this section are used to support the dramatic increase in the thermoelectric performance of observed Cu-RBS relative to RBS in Section 4.4.

4.3.1 Solid-state Absorption Spectra

Solid-state absorption spectra in Figure 4.8 were also collected by spray-coating solutions of RB, RBS, Cu-RB, and Cu-RBS onto square glass slides at equal molar concentrations. The same phenomenon observed in solution is also seen in the solid-state; introducing Cu^{2+} to the solutions increases the absorption magnitude of the chromophore nearly three-fold. Additionally, a considerable blue-shift of 31 nm in the absorption maximum of RBS is seen upon coordination to Cu^{2+}, indicating that the HOMO-LUMO energy gap of RBS was decreased upon coordination to Cu^{2+}. To calculate the energy gaps, two points of the onset of absorption spectrum were identified for each spectrum, and a straight line was extrapolated to intersect with the baseline. This point of intersect was taken to be the highest photon wavelength necessary to initiate excitation, i.e. the minimum energy necessary to excite an electron from the HOMO to the LUMO.[103] The energies calculated from the onset absorption wavelength are reported in Table 4.2, the uncertainties for which are calculated from the wavelength scanning interval of 0.5 nm. Introducing Cu^{2+} to RB showed a minor effect on the E_g, which

decreased from 2.00 eV to 1.98 eV. This provided strong evidence that Cu^{2+} induced a minor influence on the solid-state RB system. A more drastic effect was observed when Cu^{2+} was introduced to the RBS system, causing a decrease in the E_g from 2.07 eV to 2.00 eV. This is attributed to the two occupied Cu^{2+} energy levels made available to RBS by coordination to the metal ion, as discussed in Section 4.2.3.

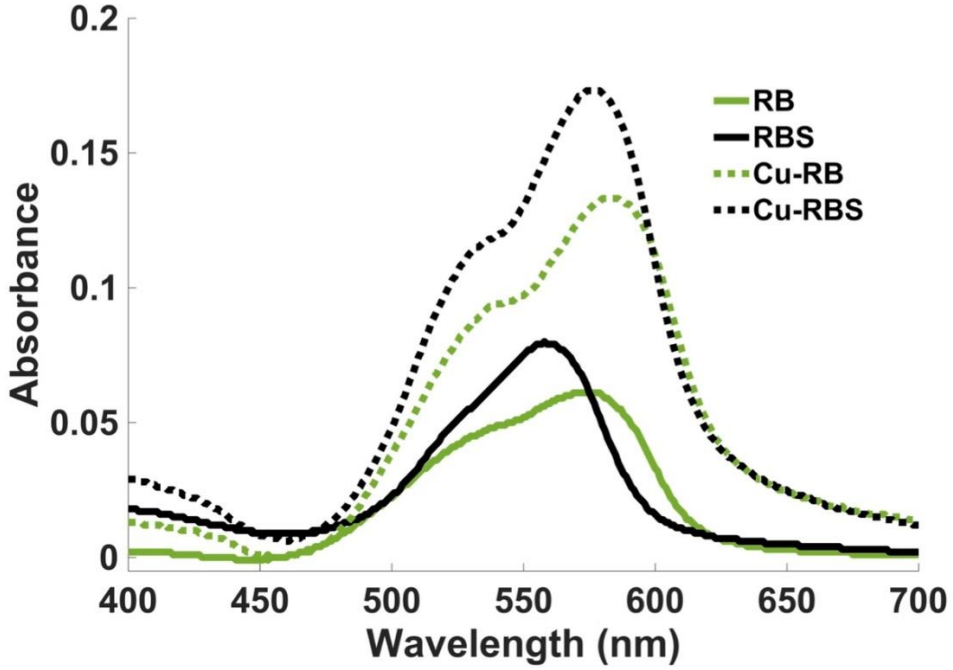

Figure 4.8: The thin film absorption spectra of RB, RBS, Cu-RB, and Cu-RBS.

Table 4.2: Summary of optical and calculated band gap energies and uncertainties for RBS and Cu-RBS.

Material	Optical E_g (eV) ± 0.002	Calculated E_g (eV)
RB	2.00	2.80
RBS	2.07	2.80
Cu-RB	1.98	2.33
Cu-RBS	2.00	2.29

4.3.2 Electrostatic Potential Surfaces of Cu-RBS and RBS

A second, less prominent peak was observed as a shoulder to the main absorption peak and occurs near ~500 nm for the thin films. This is a well-characterized phenomenon attributed to dimer formation of the dye molecules in solution, which is commonly observed for small molecule systems such as RB.[104] For RBS, this shoulder peak was less pronounced in the thin film absorption spectrum than Cu-RBS. To provide insight into this observation, electrostatic potential (ESP) surfaces were generated and dipole moments were recorded for RBS and Cu-RBS from computational simulations (Figure 4.9). In comparison to RBS (Figure 4.9(a)), much of the electron density is redistributed to the silane tail away from the carboxamide group and xanthene core structure when coordination with Cu^{2+} occurred (Figure 4.9(b)). This enhanced anisotropic distribution of electron density resulted in an increase in the dipole moment of RBS from 11.248 Debye to 16.621 Debye upon coordination with Cu^{2+}. A larger dipole moment results in more consistent molecular packing in the thin-film

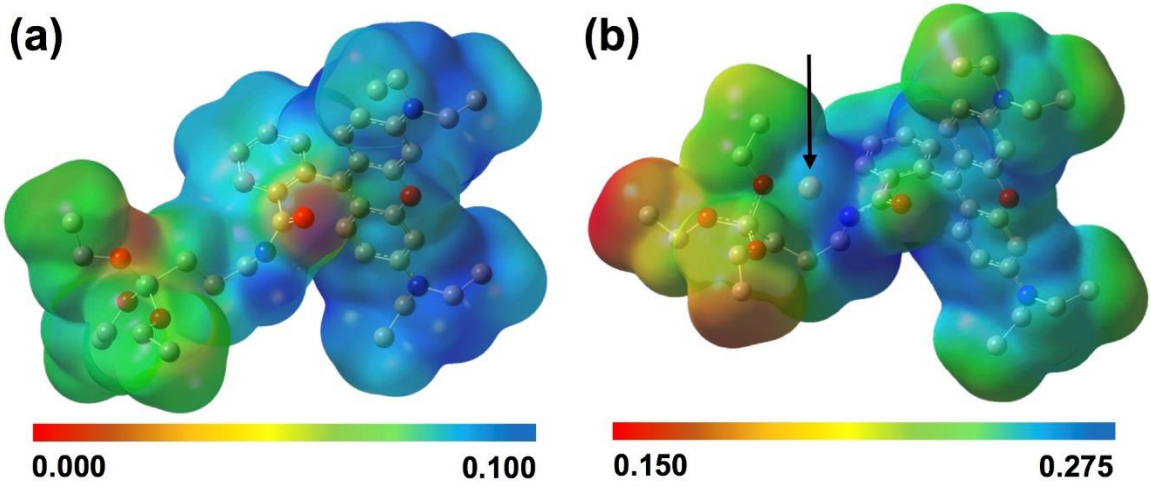

Figure 4.9: Electrostatic surface potential of (a) RBS and (b) Cu-RBS calculated using B3LYP method and LANL2DZ basis set for Cu^{2+} while /6-31G was applied to all other atoms. The black arrow indicates the position of the Cu^{2+} ion.

because of stronger intermolecular interactions. Thus, the loosely packed RBS molecules are less likely to take part in vibronic transitions resulting from dimer formation, resulting in a decreased absorbance intensity for the shoulder peak in the thin-film absorption spectrum of RBS. Additionally, the more consistent molecular packing of Cu-RBS in the thin film may increase the likelihood of electron transfer between sites on the thin-film.

4.3.3 Torsion Angles of the Chromophore

The calculated torsion angle of the phenyl amide group (or benzoic acid of RB) relative to the fused structure for RB, RBS, Cu-RB, and Cu-RBS was examined to investigate strain that the silane tail of RBS may impose on its π-conjugated structure, which could impact the likelihood of π stacking in thin films. A depiction of the change of the dihedral angle of the lone benzene ring on RB relative to the xanthene core upon silanation (RBS) and successive complexation with Cu^{2+} (Cu-RBS) is depicted in Figure 4.10. The slight decrease in the torsion angle for RBS compared to RB indicates that the attachment of the silane tail to RB does cause some torsion of the xanthene ring relative to the phenyl ring, and provides more freedom to arrange xanthene moieties with void spaces in the solid phase, thus, resulting in a blue-shift in the thin film absorption maxima of RBS compared to the absorption maxima of Cu-RBS. Upon complexation with the metal ion, the phenyl amide group reverts to a relaxed conformation like RB, thereby leading to closely packed xanthene moieties in the solid phase.

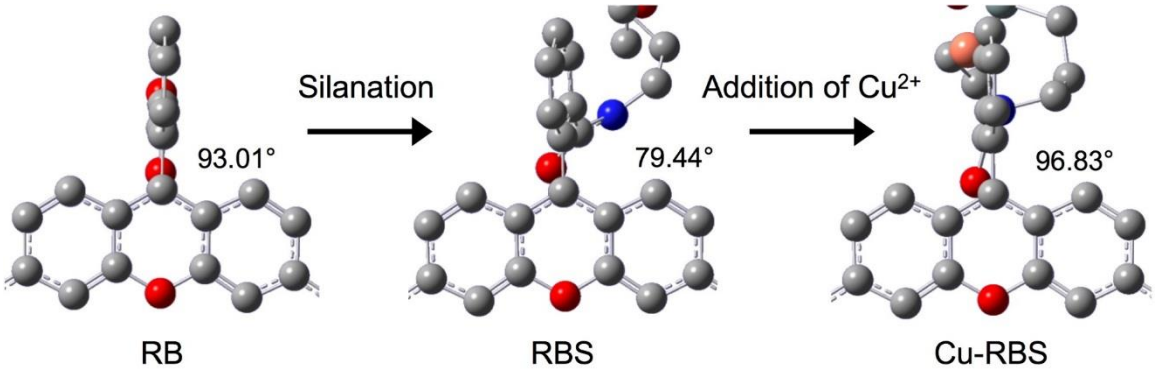

Figure 4.10: Depiction of the torsional strain placed on the lone benzene ring of RB upon attachment of the silane tail which leads to loose molecular packing in the solid state. However, upon complexation to Cu^{2+} the torsional strain is relieved. A portion of the RBS molecule is cropped out of the images for simplicity.

4.3.4 Computational HOMO-LUMO

Computational HOMO-LUMO energy gaps (E_g) were calculated from computational chemistry simulations using the B3LYP method and 6-31G basis set, while LANL2DZ basis was applied to Cu^{2+} atoms only. Two sets of singly occupied molecular orbitals (SOMOs) with α- and β-spin electrons were calculated for Cu-RB and Cu-RBS due to their doublet spin-multiplicity. A single E_g was obtained for Cu-RB and Cu-RBS by averaging the α- and β- spin E_g for each species. Table 4.2 summarizes these energies for RB, RBS, Cu-RB, and Cu-RBS. A theoretical E_g of 2.80 eV was found for RB and RBS, which is validated by the fact that both possessed the same frontier molecular orbital contours predicted by computational methods. This indicates that addition of the silane tail to RB does little to affect its frontier molecular orbitals, and therefore, should not affect its electronic properties to a large extent. A significant decrease in the predicted E_g is predicted for Cu-RB compared to RB alone, decreasing by 0.47 eV. However, if complexation was in fact occurring between Cu^{2+} and RB, this large

decrease in the E_g should have been observed in the solid-state absorption data as it was observed for RBS and Cu-RBS.

4.4 Thermoelectric Properties

Typically, the *ZT* (Eq. 1.3) is used to measure the viability of a thermoelectric material, but in cases where measuring the thermal conductivity (κ) is not feasible, the power factor (numerator of the *ZT*) is sufficient for approximating its performance. Thus, the electrical conductivity at increasing temperatures and the Seebeck coefficient were measured for thin film devices to calculate the power factor of this novel species. The results are presented in the following section, and exhibit a new route to increasing thermoelectric performance in small-molecule systems by forming an organic/inorganic complex.

4.4.1 Electrical Conductivity

Electrical conductivity (σ) of RB, RBS, Cu-RB, and Cu-RBS as thin films were evaluated using indium tin oxide (ITO) coated glass as an anode and a copper thin film as a cathode by maintaining the cell area and channel length at 1.5 cm^2 and 1.25 cm, respectively. The current-voltage (I-V) curves were collected and are depicted in Figure 4.11(a). The I-V curves show ohmic behavior from -1 to +1 V, indicating the number of mobile charge carriers remains the same throughout the applied voltage. Addition of Cu^{2+} into solutions of RB showed only a minor improvement towards resistance reduction of the thin-film. In contrast, the Cu-RBS thin film shows a significant decrease in resistance over RBS thin film, more than doubling its current under the applied voltage range. The respective σ values calculated from Equation 2.1 are shown in Table 4.3. The

Table 4.3: Comparison of the electrical conductivities of RB, Cu-RB, RB and RBS with $Ca(NO_3)_2$, as well as RBS and Cu-RBS devices at room temperature.

Thin Film Active Layer	σ (S m^{-1})
RB	2.75 ± 0.7
RBS	2.12 ± 0.5
Cu-RB	2.87 ± 0.2
Cu-RBS	4.38 ± 0.2
RB with Ca^{2+}	2.56 ± 0.4
RBS with Ca^{2+}	3.04 ± 0.6

reproducibility of conductivities for each device was evaluated by fabricating multiple devices and performing the same measurements. Addition of Cu^{2+} to RB solutions slightly improved the average σ, from 2.75 S m^{-1} to 2.87 S m^{-1}, but standard deviations indicate that the differences in these results and not statistically significant. Thus, the addition of Cu^{2+} ions had minimal effects on the conductivity of RB.

The average σ value for RBS, 2.12 S m^{-1}, was found to be lower than RB. This provides further evidence that RBS molecules are packing loosely in the thin-film, which was initially made evident by the decreased prominence of the shoulder peak observed in its thin-film absorption spectrum (Figure 4.4(a)), causing an increase in electrical resistance. However, upon the addition of Cu^{2+} to RBS solution, the σ more than doubled, increasing from 2.12 S m^{-1} to 4.38 S m^{-1}. The increase in σ supports the decreased band gap of RBS upon addition of Cu^{2+}, made evident by optical and computational investigative methods. Thus, the population of excitable electrons made available increases through complexation of RBS to Cu^{2+}. To confirm that the

conductivity increase is indeed due to MLCT and not due to ionic strength, conductivity of RB and RBS with the addition of a non-transition metal cation, Ca^{2+}, was investigated. The σ data obtained for these two sets of devices showed only minor influences, exhibiting a slight decrease in the σ of RB and slightly increasing the σ of RBS. But, both variations of σ for RB and RBS in the presence of Ca^{2+} are within standard deviations of one another, and thus, can be regarded as a negligible effect. Therefore, these findings support the claim that the higher σ of Cu-RBS devices is due to the effective MLCT from Cu^{2+} to RBS without geometrical perturbation to the π-π stacking of the xanthene cores in thin-films. The temperature-dependent σ of Cu-RBS was calculated from the I-V curves collected from the same set of devices; results are depicted in Figure 4.11(b). The respective σ gradually decreased with increasing temperature. The moderate σ of 3.68 S m^{-1} was maintained at 90 °C, above which the value dropped significantly. It is likely that upon heating, film defects and phase segregation within the thin-films occur and results in an increased electrical resistance.

4.4.2 Seebeck Coefficient

The Seebeck coefficient (*S*) for Cu-RBS and Cu-RB obtained from the slopes of the voltage measurements as a function of increasing temperature gradient (Figure 4.11(c)) was found to be -26.2 μV/K and -5.3 μV/K, respectively (Table 4.4). The considerably larger *S* for Cu-RBS compared to Cu-RB suggests that other conductive Schiff-bases, like RBS, that have been used as a thermoelectric material may yield substantially higher *S* values when subjected to complexation with transition metal-ion species. The power factor, which gives an adequate approximation of the thermoelectric

performance of a material when finding κ is not feasible, was also calculated for Cu-RBS at room temperature and 90 °C. The power factors obtained for Cu-RBS and Cu-RB are reported in Table 4.4. The reported uncertainties are standard deviations propagated from five σ measurements for each device. The power factors obtained for Cu-RBS are significantly lower compared to the power factors of leading organic/inorganic hybrid systems such as Cu and 7,7,8,8-tretracyano-*p*-quinodomethane (2.5 $\mu W \cdot m^{-1} \cdot K^{-2}$ at 370 K)[64] and polyaniline Bi_2Te_3 nanoparticle thin-films (85 $\mu W \cdot m^{-1} \cdot K^{-2}$ at 370 K).[105] Despite this, these findings do offer a new strategy for improving the thermoelectric performance of small-molecule organic systems by undergoing coordination with a transition metal ion. This is particularly useful in organic materials that possess *n*-type conductivity, since increasing their charge carrier concentration by previously reported methods has proven challenging.

Table 4.4: Seebeck Coefficients and Power Factors for Cu-RB and Cu-RBS.

Materials	S ($\mu V \cdot K^{-1}$)	PF ($\times 10^{-3}$ $\mu W \cdot m^{-1} \cdot K^{-2}$)	
		RT (± 0.5)	90° C (± 0.35)
Cu-RB	-5.3	0.08	-
Cu-RBS	-26.2	3.0	2.4

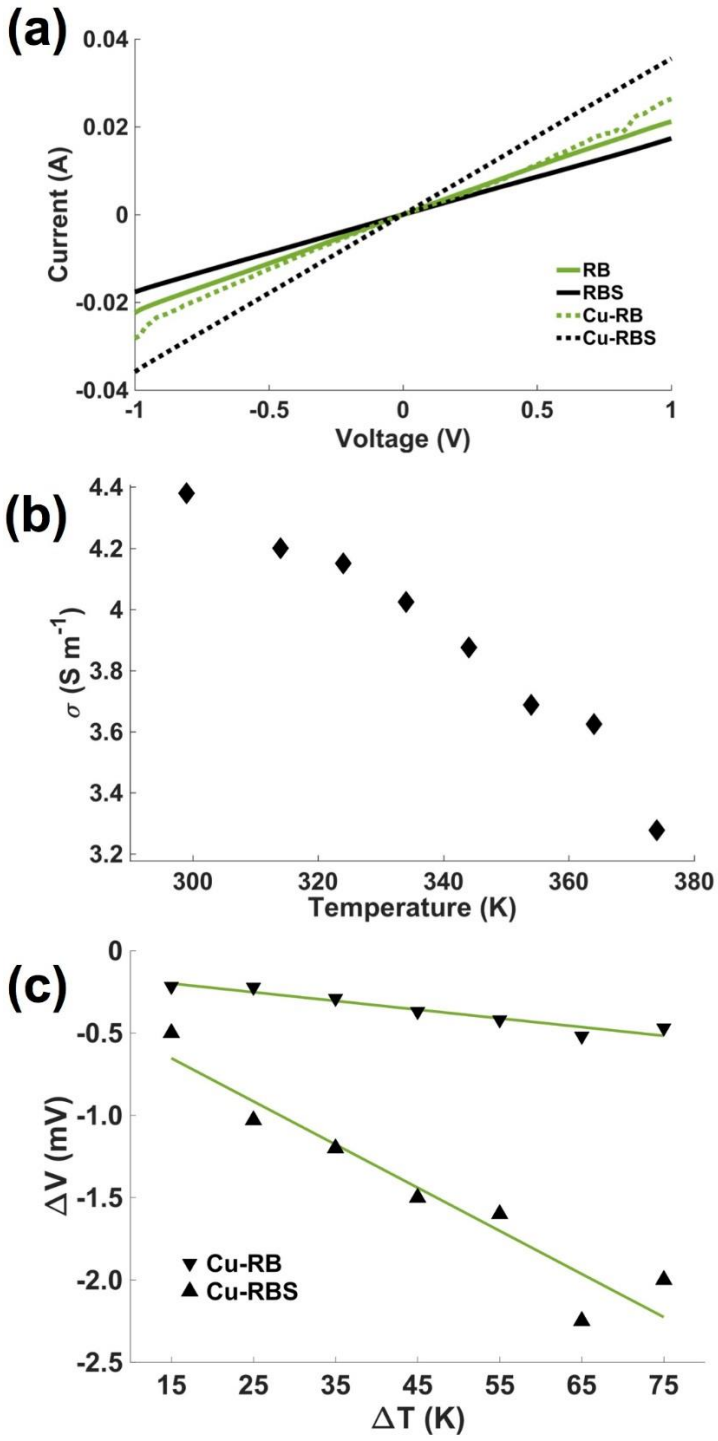

Figure 4.11: (a) Representative IV curves of test devices with RB, RBS, Cu‑RB, and Cu‑RBS as the active layer. Measurements were taken at room temperature (25 °C). (b) Measured electrical conductivity (σ) of Cu‑RBS thermoelectric device at various elevated temperatures. (c) Voltage difference measured (ΔV) under a given temperature gradient (ΔT) for Cu‑RB and Cu‑RBS at room temperature. Slopes indicated by the linear fits are used to elucidate the reported Seebeck coefficient values.

CHAPTER V

Conclusion

Two novel materials have been fabricated: Cu-RBS as a thin film for flexible thermoelectric devices, and TiO_2/PDMS beads as buoyant photocatalysts for water remediation. The results, presented along with characterization and thorough investigation of both materials, provide significant contributions to both fields that future researchers may use to analyze or improve material design in the future. Moreover, the materials themselves have many routes to be explored that could improve their performance.

5.1 Summary Statements

It has been shown that the morphology of PDMS beads can be drastically altered by the addition of an inexpensive salt, $ZnCl_2$, into the aqueous phase of the emulsion. The dependence of this effect on the salt concentration suggests that at a certain electrolyte concentration the PDMS microbubbles become unstable and aqueous domains form within the aliphatic (i.e., polymer-containing) phase. It is made apparent by the effects of NaCl on the bead morphology, which would not be expected to have a catalytic-role, that there is an advantage when metal ions known to catalyze hydrosilylation reactions are present in the emulsion. This allows beads produced with aqueous $ZnCl_2$ to achieve an increased SAV ratio by a factor of 30 compared to pristine PDMS beads.

The fabrication of a buoyant and discrete photocatalyst has also been demonstrated by anchoring anatase TiO_2 nanoparticles to the surface of PDMS beads by incorporating them into the emulsion prior to heat-curing. The high adsorption of MB to the TiO_2/PDMS beads allows a relatively low load of photocatalyst to achieve high

quality degradation of MB from solution. This keeps the analyte in proximity of the photocatalyst, which will lead to more interactions with electrons and holes generated at its surface. The discrete morphology of the beads only slightly inhibits degradation of the pollutant by direct photolysis, a complication that might inhibit removal for suspensions of free photocatalysts or non-UV-transparent polymer sheets. Additionally, the reusability of the TiO_2/PDMS beads is strong, exhibiting only minor deviations in their removal of MB by photooxidative species after five consecutive trials.

The kinetic model used in this work is significant in that it has the capacity to isolate a rate constant, k_{PO}, which solely represents how quickly the degradation target is being removed by photooxidative species generated by the photocatalyst. No previous works presenting buoyant photocatalysts in the literature have taken this approach, however, reporting k_{PO} for any buoyant photocatalyst (using the same photocatalyst and the same load of photocatalyst) could provide a means of comparing the performance of the buoyant substrates themselves.

A novel *n*-type organic/inorganic hybrid coordination complex (Cu-RBS) was synthesized from an organosiloxane-RB derivative (RBS) and Cu^{2+} for room temperature thermoelectric applications. Cu-RBS exhibited an increase in thermoelectric properties compared to RBS which is attributed to the increased charge carrier population made available by occupied electronic energy levels of Cu^{2+} lying just above HOMO levels of RBS observed in DFT calculations, allowing participation in MLCT. Although the Seebeck coefficient of $-26.2\ \mu V \cdot K^{-1}$ was the same order of magnitude as similar complexes reported in the literature, the relatively small electrical conductivity of the Cu-RBS thin films indicates that these devices are not immediately ready for practical

applications, made evident by the low power factor. Despite this, these findings offer a new strategy for improving the thermoelectric performance of small‐molecule organic systems by undergoing coordination with a transition metal ion. It is desirable to improve the properties of thermoelectric systems comprised of ubiquitous dye‐based organic species, such as RB, because they are readily available and inexpensive.

5.2 Future Outlook

The new approach to buoyant photocatalysts described here has many routes of expansion that will be explored in the future. The bead surface morphology will be altered by including soluble electrolytes, such as $ZnCl_2$, which have been proven to increase the SAV ratio. This would allow a larger fraction of the inoculated TiO_2 to exist preferentially at the PDMS substrate surface, increasing the photocatalytic activity of the beads. Another future study will be to incorporate alternative photocatalysts such as ZnO or N‐doped TiO_2, which would allow for direct comparison of PDMS beads to buoyant substrates used in other work and potentially boost removal performance. While TiO_2 was selected because it is well‐studied, inexpensive, and widely used, the methods described here could be applied to a wide variety of photocatalysts such as WO_3, ZnS, and CdS to deploy them when a buoyant substrate is needed. Additionally, alternative pollutants will be targeted including insoluble organic species to assess the TiO_2/PDMS beads performance when pollutants present themselves as slicks on bodies of water.

Implementation of the ionic conductive species RBS and the largely nonpolar conductive species POSS‐ANT into separate phases of the PDMS emulsion proved successful in terms of creating a bulk heterojunction on the microscale within the polymeric bead’s structure. Despite their inability to facilitate charge carrier flow under

an applied voltage, the approach employed to create a bulk heterojunction on the microscale is novel and could be used in future work to significantly increase power output for solar cells or thermoelectric materials which depends on the number of *p*- and *n*-type junctions present in the material's solid matrix.

Electrical conductivity of Cu-RBS thin films could be improved in several different ways. Crystallization of the complex into a conducting network such as nanowires or nanorods would improve charger carrier transfer through the film, effectively reducing the resistance and therefore increasing the electrical conductivity. Varying deposition methods could also be pursued, such as spin-coating, drop-casting, or chemical vapor deposition, which could increase the homogeneity of the thin film, allowing a decrease in electrical resistance. Additionally, attempts will be made to coordinate alternative metal ions into the organosiloxane system, particularly those which have exhibited formidable thermoelectric performance in other materials, such as Pb^{2+} and Bi^{3+} to further improve this material's performance. This work has been presented with hope that future researchers will implement the demonstrated strategies to improve the performance of both buoyant photocatalyst materials and small-molecule organic thermoelectric systems.

Bibliography

(1) Rawat, D.; Mishra, V.; Sharma, R. S. *Chemosphere* **2016**, *155*, 591–605.

(2) Taamallah, A.; Merouani, S.; Hamdaoui, O. *Desalin. Water Treat.* **2016**, *57*, 27314–27330.

(3) Jain, R.; Mathur, M.; Sikarwar, S.; Mittal, A. *J. Environ. Manage.* **2007**, *85*, 956–964.

(4) Dariani, R. S.; Esmaeili, A.; Mortezaali, A.; Dehghanpour, S. *Optik* **2016**, *127*, 7143–7154.

(5) Alizadeh, M.; Aminzadeh, B.; Vahidi, H. *Environ. Tech.* **2013**, *34*, 1183–1190.

(6) Okamoto, K.; Yamamoto, Y.; Tanaka, H.; Tanaka, M.; Itaya, A. *Bull. Chem. Soc. Jpn.* **1985**, *58*, 2015–2022.

(7) Wang, L.; Zhang, F.; Lin, F.; Zhang, Y. T.; Xue, X.; Liang, X.; Xu, O. *Environ. Sci. Technol.* **2007**, *41*, 3747–3751.

(8) Altın, İ.; Sökmen, M. *CLEAN* **2015**, *43*, 1025–1030.

(9) Asahi, R.; Morikawa, T.; Irie, H.; Ohwaki, T. *Chem. Rev.* **2014**, *114*, 9824–9852.

(10) Lamberti, A. *Appl. Surf. Sci.* **2015**, *335*, 50–54.

(11) Paz, Y.; Luo, Z.; Rabenberg, L.; Heller, A. *J. Mater. Res.* **1995**, *10*, 2842–2848.

(12) Fujishima, A.; Zhang, X.; Tryk, D. A. *Surf. Sci. Rep.* **2008**, *63*, 515–582.

(13) Kumar, S. G.; Devi, L. G. *J. Phys. Chem. A* **2011**, *115*, 13211–13241.

(14) Tavares, M. T. S.; Santos, A. S. F.; Santos, I. M. G.; Silva, M. R. S.; Bomio, M. R. D.; Longo, E.; Paskocimas, C. A.; Motta, F. V. *Surf. Coat. Technol.* **2014**, *239*, 16–19.

(15) Wei, M.; Konishi, Y.; Zhou, H.; Yanagida, M.; Sugihara, H.; Arakawa, H. *J. Mater. Chem.* **2006**, *16* (13), 1287–1293.

(16) Miyauchi, M.; Nakajima, A.; Watanabe, T.; Hashimoto, K. *Chem. Mater.* **2002**, *14*, 2812–2816.

(17) Bekbölet, M.; Lindner, M.; Weichgrebe, D.; Bahnemann, D. W. *Sol. Detoxif.* **1996**, *56*, 455–469.

(18) Lazar, M.; Varghese, S.; Nair, S. *Catal.* **2012**, *2*, 572–601.

(19) Mehrjouei, M.; Müller, S.; Möller, D. *J. Environ. Manage.* **2013**, *120*, 68–74.

(20) Hazen, T. C.; Dubinsky, E. A.; DeSantis, T. Z. *Science* **2010**, *330*, 208–211.

(21) Weber, R. C.; Lin, P.-Y.; Garnero, E. J.; Williams, Q.; Lognonné, P. *Science* **2011**, *331*, 312–315.

(22) Whelton, A. J.; McMillan, L.; Connell, M.; Kelley, K. M.; Gill, J. P.; White, K. D.; Gupta, R.; Dey, R.; Novy, C. *Environ. Sci. Technol.* **2015**, *49*, 813–823.

(23) Byrne, J. A.; Eggins, B. R.; Brown, N. M. D.; McKinney, B.; Rouse, M. *Appl. Catal. B* **1998**, *17*, 25–36.

(24) Singh, S.; Mahalingam, H.; Singh, P. K. *Appl. Catal. A* **2013**, *462-463*, 178–195.

(25) Singh, S.; Singh, P. K. *Int. J. Environ. Res.* **2015**, *9*, 535–544.

(26) Długosz, M.; Waś, J.; Szczubiałka, K.; Nowakowska, M. *J. Mater. Chem. A* **2014**, *2*, 6931–6938.

(27) Zhang, L.; Xing, Z.; Zhang, H.; Li, Z.; Zhang, X.; Zhang, Y.; Li, L.; Zhou, W. *Chempluschem* **2014**, *80*, 623–629.

(28) Singh, S.; Singh, P. K.; Mahalingam, H. *Ind. Eng. Chem. Res.* **2014**, *53*,

16332–16340.

(29) Han, H.; Bai, R. *Sep. Purif. Technol.* **2010**, *73*, 142–150.

(30) Tu, W.; Lin, Y.-P.; Bai, R. *Sep. Purif. Technol.* **2013**, *115*, 180–189.

(31) Xu, H.; Zhu, P.; Wang, L.; Jiang, Z.; Zhao, S. *J. Wuhan Univ. Technol.-Mat. Sci. Edit.* **2016**, *31*, 80–86.

(32) Wan, W.; Yu, S.; Dong, F.; Zhang, Q.; Zhou, Y. *J. Mater. Chem. A* **2016**, *4*, 7823–7829.

(33) Bertram, J. R.; Nee, M. J. *J. Vis. Exp.* **2015**, *106*, e53440.

(34) Farmer, B. C.; Mason, M. A.; Nee, M. J. *Mater. Lett.* **2013**, *98*, 105–107.

(35) Dufaud, O.; Favre, E.; Sadtler, V. *J. Appl. Polym. Sci.* **2001**, *83*, 967–971.

(36) Vrana, B.; Popp, P.; Paschke, A.; Schüürmann, G. *Anal. Chem.* **2001**, *73*, 5191–5200.

(37) Kim, T.-Y.; Alhooshani, K.; Kabir, A.; Fries, D. P.; Malik, A. *J. Chromatogr. A* **2004**, *1047*, 165–174.

(38) Park, I.; Efimenko, K.; Sjoblom, J.; Genzer, J. *J. Dispers. Sci. Technol.* **2009**, *30*, 318–327.

(39) Li, N.; Li, T.; Lei, X.; Fu, B.; Liao, W.; Qiu, J. *Polym. Eng. Sci.* **2014**, *54*, 2965–2969.

(40) Zhang, A. J.; Chen, M. J.; Du, C.; Guo, H. Z.; Bai, H.; Li, L. *ACS Appl. Mater. Interfaces* **2013**, *5*, 10201–10206.

(41) Silva, V. P.; Paschoalino, M. P.; Gonçalves, M. C.; Felisberti, M. I.; Jardim, W. F.; Yoshida, I. V. P. *Mater. Chem. Phys.* **2009**, *113*, 395–400.

(42) Zhao, Y.; Liu, Y.; Xu, Q.; Barahman, M.; Lyons, A. M. *ACS Appl. Mater.*

Interfaces **2015**, *7*, 2632–2640.

(43) Lisensky, G. C.; Campbell, D. J.; Beckman, K. J.; Calderon, C. E.; Doolan, P. W.; Rebecca M Ottosen; Ellis, A. B. *J. Chem. Educ.* **1999**, *76*, 537–541.

(44) Zhou, Z.-L.; Sheng, X.; Nauka, K.; Zhao, L.; Gibson, G.; Lam, S.; Yang, C. C.; Brug, J.; Elder, R. *Appl. Phys. Lett.* **2010**, *96*, 013504–1–013504–3.

(45) Dun, C.; Hewitt, C. A.; Huang, H.; Montgomery, D. S.; Xu, J.; Carroll, D. L. *Phys. Chem. Chem. Phys.* **2015**, *17*, 8591–8594.

(46) Dun, C.; Hewitt, C. A.; Huang, H.; Xu, J.; Montgomery, D. S.; Nie, W.; Jiang, Q.; Carroll, D. L. *ACS Appl. Mater. Interfaces* **2015**, *7*, 7054–7058.

(47) Culebras, M.; Gómez, C.; Cantarero, A. *Materials* **2014**, *7*, 6701–6732.

(48) Seebeck, T. J. *Abh. Akad. Wiss.* **1822**, 289–346.

(49) Ioffe, A. F. *Semiconductor Thermoelements and Thermoelectric Cooling*; London, 1957.

(50) Shakouri, A. *Annu. Rev. Mater. Res.* **2011**, *41*, 399.

(51) Franz, R.; Wiedemann, G. *Annalen der Physik* **1853**, *165*, 497–531.

(52) Vining, C. B. *Nat. Mater.* **2009**, *8*, 83–85.

(53) Janata, J.; Josowicz, M. *Nat. Mater.* **2003**, *2*, 19–24.

(54) Xiao, H.; Qiu, K.; Gou, X.; Ou, Q. *Applied Energy* **2013**, *112*, 1161–1165.

(55) Carno, J. P.; Goncalves, L. M.; Correia, J. H. *IEEE Trans. Ind. Electron.* **2010**, *57*, 861–867.

(56) Shi, W.; Chen, J.; Xi, J.; Wang, D.; Shuai, Z. *Chem. Mater.* **2014**, *26*, 2669–2677.

(57) Nakamura, H.; Ohto, T.; Ishida, T.; Asai, Y. *J. Am. Chem. Soc.* **2013**, *135*,

16545–16552.

(58) Leu, C. M.; Chang, Y. T.; Wei, K. H. *Chem. Mater.* **2003**, *15*, 3721–3727.

(59) Toshima, N. *Macromol. Symp.* **2002**, *186*, 81–86.

(60) Yan, H.; Sada, N.; Toshima, N. *J. Therm. Anal. Calorim.* **2002**, *69*, 881–887.

(61) Kim, G. H.; Shao, L.; Zhang, K.; Pipe, K. P. *Nat. Mater.* **2013**, *12*, 719–723.

(62) Huang, D.; Wang, C.; Zou, Y.; Shen, X.; Zang, Y.; Shen, H.; Gao, X.; Yi, Y.; Xu, W.; Di, C.-A.; Zhu, D. *Angew. Chem.* **2016**, *128*, 10830–10833.

(63) Wan, C.; Gu, X.; Dang, F.; Itoh, T.; Wang, Y.; Sasaki, H.; Kondo, M.; Koga, K.; Yabuki, K.; Snyder, G. J.; Yang, R.; Koumoto, K. *Nat. Mater.* **2015**, *14*, 622–627.

(64) Sun, Y.; Zhang, F.; Sun, Y.; Di, C.-A.; Xu, W.; Zhu, D. *J. Mater. Chem. A* **2015**, *3*, 2677–2683.

(65) Sun, Y.; Sheng, P.; Di, C.; Jiao, F.; Xu, W.; Qiu, D.; Zhu, D. *Adv. Mater.* **2012**, *24*, 932–937.

(66) Tian, R.; Wan, C.; Wang, Y.; Wei, Q.; Ishida, T.; Yamamoto, A.; Tsuruta, A.; Shin, W.; Li, S.; Koumoto, K. *J. Mater. Chem. A* **2016**, *5*, 564–570.

(67) Bredas, J. L.; Silbey, R.; Bourdeaux, D. S.; Chance, R. R. *J. Am. Chem. Soc.* **1983**, *105*, 6555–6559.

(68) Pfeiffer, M.; Beyer, A.; Fritz, T.; Leo, K. *Appl. Phys. Lett.* **1998**, *73*, 3202.

(69) Pernstich, K. P.; Batlogg, B.; Rossner, B. *Nat. Mater.* **2008**, *7*, 321–325.

(70) Hayashi, K.; Shinano, T.; Miyazaki, Y.; Kajitani, T. *J. Appl. Phys.* **2011**, *109*, 023712.

(71) Harada, K.; Sumino, M.; Adachi, C.; Tanaka, S.; Miyazaki, K. *Appl. Phys. Lett.*

2010, *96*, 253304.

(72) Kim, G. H.; Shtein, M.; Pipe, K. P. *Appl. Phys. Lett.* **2011**, *98*, 093303.

(73) Sedghi, G.; García-Suárez, V. M.; Esdaile, L. J.; Anderson, H. L.; Martín, S.; Bethell, D.; Higgins, S. J.; Elliott, M.; Bennett, N.; Macdonald, J. E.; Nichols, R. J. *Nat. Nanotechnol.* **2011**, *6*, 517–523.

(74) Tuccitto, N.; Ferri, V.; Cavazzini, M.; Quici, S.; Zhavnerko, G.; Licciardello, A.; Rampi, M. A. *Nat. Mater.* **2009**, *8*, 41–46.

(75) Luo, L.; Benameur, A.; Brignou, P.; Choi, S. H.; Rigaut, S.; Frisbie, C. D. *J. Phys. Chem. C* **2011**, *115*, 19955–19961.

(76) Meng, X.; Xu, Y.; Liu, J.; Sun, L.; Shi, L. *Anal. Methods* **2016**, *8*, 1044–1051.

(77) Mei, L.; Xiang, Y.; Li, N.; Tong, A. *Talanta* **2007**, *72*, 1717–1722.

(78) Pires, S. M. G.; Núñez, C.; Serra, V. V.; Sánchez-Coronilla, A.; Faustino, M. A. F.; Simões, M. M. Q.; Silva, A. M. S.; Neves, M. G. P. M. S.; Capelo, J. L.; Lodeiro, C. *Dyes Pigm.* **2016**, *135*, 113–126.

(79) Bertram, J. R.; Penn, A.; Nee, M. J.; Rathnayake, H. *ACS Appl. Mater. Interfaces* **2017**, *9*, 10946–10954.

(80) Huzyak, P.; Ferguson, J.; Sharpensteen, J.; Xu, L.; Ananthakrishnan, S. J.; Rathnayake, H. *RSC Adv.* **2015**, *5*, 37859–37868.

(81) *Gaussian 09, Revision A.08*: Frisch, M. J.; Trucks, G. W.; Schlegel, H. B.; Scuseria, G. E.; Robb, M. A.; Cheeseman, J. R.; Scalmani, G.; Barone, V.; Mennucci, B.; Petersson, G. A.; Nakatsuji, H.; Caricato, M.; Li, X.; Hratchian, H. P.; Izmaylov, A. F.; Bloino, J.; Zheng, G.; Sonnenberg, J. L.; Hada, M.; Ehara, M.; Toyota, K.; Fukuda, R.; Hasegawa, J.; Ishida, M.; Nakajima, T.;

Honda, Y.; Kitao, O.; Nakai, H.; Vreven, T.; Montgomery, J. A. J.; Peralta, J. E.; Ogliaro, F.; Bearpark, M.; Heyd, J. J.; Brothers, E.; Kudin, K. N.; Staroverov, V. N.; Kobayashi, R.; Normand, J.; Raghavachari, K.; Rendell, A.; Burant, J. C.; Iyengar, S. S.; Tomasi, J.; Cossi, M.; Rega, N.; Millam, J. M.; Klene, M.; Knox, J. E.; Cross, J. B.; Bakken, V.; Adamo, C.; Jaramillo, J.; Gomperts, R.; Stratmann, R. E.; Yazyev, O.; Austin, A. J.; Cammi, R.; Pomelli, C.; Ochterski, J. W.; Martin, R. L.; Morokuma, K.; Zakrzewski, V. G.; Voth, G. A.; Salvador, P.; Dannenberg, J. J.; Dapprich, S.; Daniels, A. D.; Farkas, Ö.; Foresman, J. B.; Ortiz, J. V.; Cioslowski, J.; Fox, D. J. Gaussian, Inc.: Wallingford, CT, 2009.

(82) Dennington, R.; Keith, T.; Milliam, J. *Gaussview Version 5*; Semichem, Inc.: Shawnee Mission, KS, 2009.

(83) Stephens, P. J.; Devlin, F. J.; Chabalowski, C.; Frisch, M. J. *J. Phys. Chem.* **1994**, *98*, 11623–11627.

(84) Ditchfield, R.; Hehre, W. J.; Pople, J. A. *J. Chem. Phys.* **1971**, *54*, 724–728.

(85) Hay, P. J.; Wadt, W. R. *J. Phys. Chem.* **1985**, *82*, 270–283.

(86) Cifuentes, M. E.; Strong, M. R.; Vanwert, B. 1999.

(87) Balachandran, U.; Eror, N. G. *J. Solid State Chem.* **1982**, *42*, 276–282.

(88) Forgacs, E.; Cserháti, T.; Oros, G. *Environ. Int.* **2004**, *30*, 953–971.

(89) Houas, A.; Lachheb, H.; Ksibi, M.; Elaloui, E. *Appl. Catal. B* **2001**, *31*, 145–157.

(90) Srikant, V.; Clarke, D. R. *J. Appl. Phys.* **1998**, *83*, 5447–5451.

(91) Li, H.; Hao, Y.; Lu, H.; Liang, L.; Wang, Y.; Qiu, J.; Shi, X.; Wang, Y.; Yao, J.

Appl. Surf. Sci. **2015**, *344*, 112–118.

(92) Fatin, S. O.; Lim, H. N.; Tan, W. T.; Huang, N. M. *Int. J. Electrochem. Sci.* **2012**, *7*, 9074–9084.

(93) Sakthivel, S.; Neppolian, B.; Shankar, M. V.; Arabindoo, B.; Palanichamy, M.; Murugesan, V. *Sol. Energy Mater. Sol. Cells* **2003**, *77*, 65–82.

(94) Fouad, O. A.; Ismail, A. A.; Zaki, Z. I.; Mohamed, R. M. *Appl. Catal. B* **2006**, *62*, 144–149.

(95) Mulliken, R. S. *J. Chem. Phys.* **1955**, *23*, 1833–1840.

(96) Griffith, J. S.; Orgel, L. E. *Q. Rev. Chem. Soc.* **1957**, *11*, 381.

(97) Zhang, W.; Tang, B.; Liu, X.; Liu, Y.; Xu, K.; Ma, J.; Tong, L.; Yang, G. *Analyst* **2009**, *134*, 367–371.

(98) Gaur, A.; Klysubun, W.; Nitin Nair, N.; Shrivastava, B. D.; Prasad, J.; Srivastava, K. *J. Mol. Struct.* **2016**, *1118*, 212–218.

(99) Sadhukhan, D.; Ray, A.; Das, S.; Rizzoli, C.; Rosair, G. M.; Mitra, S. *J. Mol. Struct.* **2010**, *975*, 265–273.

(100) Bethe, H. *Ann. Phys.* **1929**, *3*, 133.

(101) Miessler, G. L.; Tarr, D. A. *Inorganic Chemistry. Pearson Education*; Upper Saddle River, 2004; pp 393–394.

(102) Jahn, H. A.; Teller, E. *Proc. R. Soc. A: Math. Phys. Eng. Sci.* **1937**, *161*, 220–235.

(103) Schlaf, R.; Schroeder, P. G.; Nelson, M. W.; Parkinson, B. A.; Merritt, C. D.; Crisafulli, L. A.; Murata, H.; Kafafi, Z. H. *Surf. Sci.* **2000**, *450*, 142–152.

(104) Chambers, R. W.; Kearns, D. R. *J. Phys. Chem.* **1968**, *72*, 4718–4720.

(105) Dubey, N.; Leclerc, M. *J. Polym. Sci. B Polym. Phys.* **2011**, *49*, 467–475.